Reviews of Geophysics

REVIEW ARTICLE
10.1029/2020RG000703

Key Points:
- Churn flow upstream of the orifice due to the presence of oil and gas, formation of compound droplets, and tip streaming is highlighted
- Experiments of oil jets up to centimeters scale orifices were obtained, and engineering-type models were calibrated to them
- Integral plume models including thermodynamics and chemistry of phases led to complete quantification of mass and heat transfer rates

Supporting Information:
- Supporting Information S1

Correspondence to:
M. C. Boufadel,
boufadel@gmail.com

Citation:
Boufadel, M. C., Socolofsky, S., Katz, J., Yang, D., Daskiran, C., & Dewar, W. (2020). A review on multiphase underwater jets and plumes: Droplets, hydrodynamics, and chemistry. *Reviews of Geophysics*, *58*, e2020RG000703. https://doi.org/10.1029/2020RG000703

Received 4 MAR 2020
Accepted 8 JUL 2020
Accepted article online 20 JUL 2020

©2020. American Geophysical Union. All Rights Reserved.

A Review on Multiphase Underwater Jets and Plumes: Droplets, Hydrodynamics, and Chemistry

Michel C. Boufadel[1], Scott Socolofsky[2], Joseph Katz[3], Di Yang[4], Cosan Daskiran[1], and William Dewar[5]

[1]Center for Natural Resources, Civil and Environmental Engineering Department, New Jersey Institute of Technology, Newark, NJ, USA, [2]Zachry Department of Civil Engineering, Texas A&M University, College Station, TX, USA, [3]Department of Mechanical Engineering, Johns Hopkins University, Baltimore, MD, USA, [4]Department of Mechanical Engineering, University of Houston, Houston, TX, USA, [5]Department of Earth, Ocean and Atmospheric Science, Florida State University, Tallahassee, FL, USA

Abstract Jets and plumes have been the focus of quantitative investigations since the mid-1950s. These investigations intensified following the Deepwater Horizon oil spill, in which thousands of tons of oil and natural gas were released into the Gulf of Mexico. This review focuses on plume dynamics that apply to both single-phase and multiphase liquid-in-liquid and liquid plus gas into liquid plumes, including bubble and droplet formation, and heat and mass transfer. Broadly, our work highlights several previously unknown or overlooked aspects of multiphase flow in the deep oceans. Upstream of the jet release, multiphase hydraulics can significantly affect the turbulence, for instance, through churn flow that enhances the turbulence in the free jet, affecting the conditions where bubbles and droplets are formed. Droplet formation was a major focus recently, with experiments covering a range of scales and flow rates of oil and gas at low and high pressure. Detailed observations of droplet formation at the jet-water boundary reveal the formation of compound droplets, which are emulsions of oil and water with implications for mass conservation and mass transfer. At the plume scale, integral models have been adapted to include the complex thermodynamics and chemistry of oil and gas plumes. In parallel, significant advances were made in numerical simulations of multiphase plumes through large eddy simulations by treating the oil and gas either a continuous or discrete phase. Through this work, a vivid picture of the complex droplet, chemical, and hydrodynamic behavior of multiphase plumes in the ocean is emerging.

Plain Language Summary Interest in jet and plumes in natural systems increased since the mid-1950s. Following the Deepwater Horizon oil spill at 1,500 m depth of the Gulf of Mexico, experimental and numerical studies of jets and plumes increased to better understand hydrodynamics, chemistry, and the fate of oil droplets in the water column. This work highlights several newly discovered aspects of multiphase flows. Upstream of the jet release (inside the pipe), the increase in the gas fraction leads to chaotic and highly turbulent churn flow, which affects the conditions where bubbles and droplets are formed. Observations of droplet formation near the jet-water interface revealed the formation of composite droplets such as an oil droplet including a water droplet inside, which is important for the estimation of mass and heat transfer among the phases. At the plume scale, integral models including chemical and thermal properties of oil and gas at different ambient conditions, that is, pressure and temperature are developed. In parallel, numerical simulations of multiphase plumes with high-fidelity turbulence models are performed and compared to the measurements.

1. Introduction

The natural or accidental release of hydrocarbon liquids and gases in the form of jets and plumes underwater is an important process that impacts the subsea ecosystem and potentially the atmosphere. The main driving mechanism for the release is usually the high pressure in the reservoir (whether geologic or human made), but upon release in water, buoyancy (due to the lower density of the released fluids) eventually takes over and causes the rise of many hydrocarbons through the water column, potentially to the water surface, and ultimately to the atmosphere. Many of the processes have been poorly understood due to the hydrodynamic complexity of the release of a multiphase plume (liquid hydrocarbons and gas) (Boufadel et al., 2018; Socolofsky et al., 2002), the formation of droplets (Zhao, Shaffer, et al., 2016, Xue & Katz, 2019) and

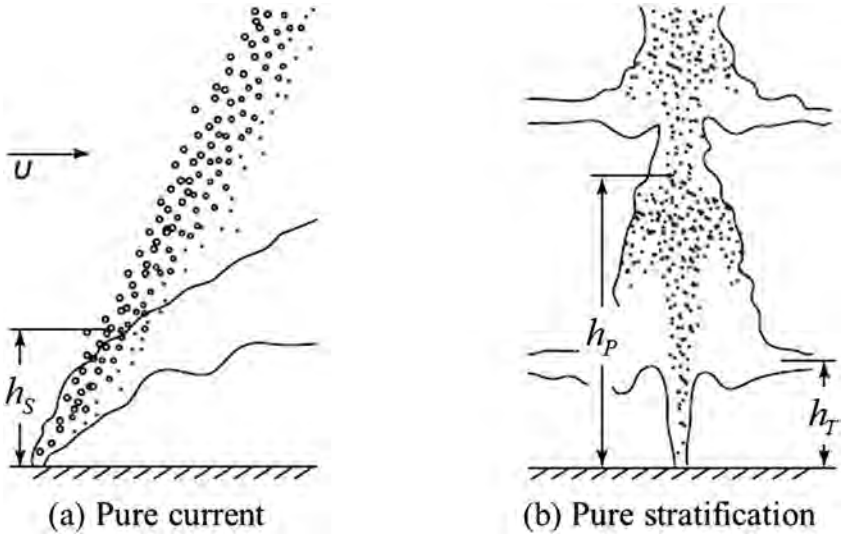

Figure 1. Behavior of droplets and bubbles within plumes exposed to (a) pure current and (b) pure stratification. Taken from Socolofsky et al. (2011).

bubbles (Leifer et al., 2015; Wang et al., 2018), and the behavior of hydrocarbon components at depth (Gros et al., 2016).

In this review, we consider the dynamics of this gas and liquid petroleum jet as it penetrates the water column, interacts with the ambient ocean, and rises to the sea surface. Throughout this review, we will often refer to the petroleum fluids as oil and gas, with "oil" denoting the liquid-phase petroleum and "gas" the gas phase. However, the actual petroleum compounds found in the liquid or gas phases change with temperature, pressure, and oil chemistry (Gros et al., 2016). We will also use the term "blowout" or "oil well blowout" to refer to those cases where an accident results in release of oil to the environment. For past such blowouts, including the Deepwater Horizon (DWH) (Gros et al., 2017; Reddy et al., 2012) and the IxtocI (Murawski et al., 2019; Patton et al., 1981), oil and gas were released from a localized source at the seafloor. Natural releases of hydrocarbon plumes underwater have been documented in various studies (Leifer et al., 2006; MacDonald et al., 2002). Regardless of the cause of the release, once the fluids enter the water body, the oil and gas experience a series of natural phenomenon as they traverse the ocean water column.

Because petroleum fluids are immiscible with water, the interface between the oil and gas and the ambient seawater quickly destabilizes, resulting in creation of a spectrum of oil droplets and gas bubbles. This begins immediately at the orifice and occurs very rapidly. The plume-scale trajectory of multiphase plumes depends on the relative importance of horizontal currents and stratification (Figure 1). When horizontal currents dominate, the gas bubbles and large droplets exit at a separation height h_S, leaving a wake of entrained seawater with dissolved and finely dispersed hydrocarbons (Figure 1a). When stratification dominates in the water column due to seawater density (Figure 1b), the plume reaches a peel height h_P, where dispersed phase buoyancy can no longer lift the entrained seawater, and the entrained seawater begins to descend, forming a lateral intrusion layer (Socolofsky et al., 2011). All of the dissolved petroleum compounds in the entrained seawater follow the peeling fluid into the intrusion layer, which eventually gets trapped at a level of neutral buoyancy (trap height), h_T (estimates of h_S, h_P, and h_T can be obtained based on the jet properties, as discussed below). Laboratory experiments suggest that the plume is dominated by horizontal currents if $h_S < h_P$ and by stratification if $h_S > h_P$ (Socolofsky & Adams, 2002). While dissolved plumes in stratification forms only one intrusion zone, multiphase plumes, gas bubbles and oil droplets rising past the first peel height, may form a new multiphase buoyant plume with a new intrusion zone (Figure 1b).

As the plume rises, petroleum compounds dissolve into the entrained seawater from the gas bubbles and liquid oil droplets, and some may remain as a separate phase (i.e., not dissolved) and reach the water surface, and may continue to the atmosphere (Leifer et al., 2006). In the shallow Ixtoc I blowout (50 m water depth), nearly all of the gas escaped to the atmosphere and created a continuous fire above the blowout. For the

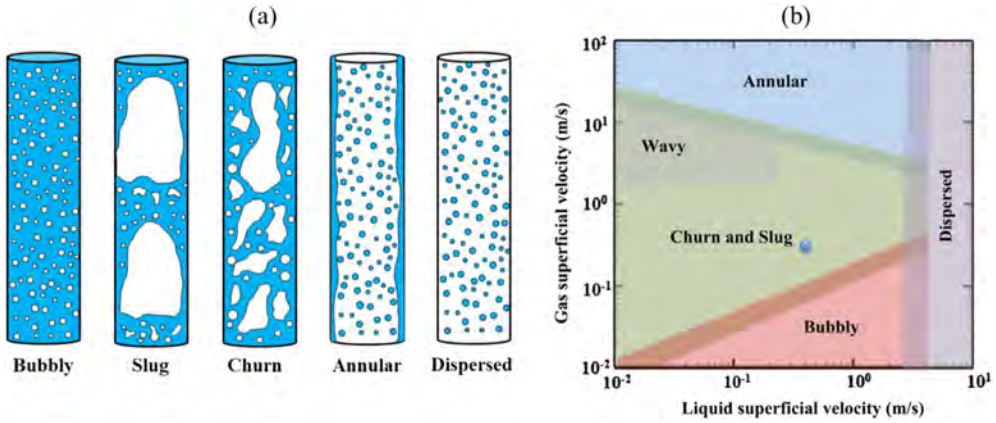

Figure 2. (a) Schematic of the multiphase flow regimes in a vertical pipe. (b) Flow regime "map" adapted from Weisman (1983) including transition regimes. Wavy flow is a special case of churn/slug flow. The blue disk represents the Deepwater Horizon condition.

DWH, all of the gas bubbles released at the wellhead dissolved into the water column or dissolved to the point that they condensed to a liquid phase (Gros et al., 2017).

As this discussion demonstrates, the cascade of processes following a subsea oil and gas involve many fundamental thermodynamic and fluid-dynamic chemical processes occurring in other geophysical contexts. Often, the geophysical analog is at a different scale, as in oil and gas release from natural seeps or in multiphase plumes emanating from black smokers at ocean ridges, but some of the fine-scale processes remain the same. These include particle (bubble, droplet, or solid particle) interaction with ocean currents, as in gas entrainment under breaking waves, oil and gas bubble release from submarine natural seeps, and sediment transport; buoyant plume dynamics, as in volcanic eruptions, cloud physics, and black smokers, dissolution of bubbles and droplets, as for submarine natural seeps and aeration at the air-water interface.

In this review, we limit our discussion to a near-field region close to the subsea release point, where buoyancy dominates causing the plume to form and develop into a rising turbulent plume and generally ends after intrusion formation. We consider that the edge of the near-field zone is around 10 km from the source, which would allow us to assume that the vertical profiles of salinity, temperature, and currents are representative of the ocean water column within the near-field region. The midfield zone occurs at the edge of the near field and is the area where knowledge of larger-scale ocean circulation becomes important to predict the oil transport. Far-field models, which utilize temporally and spatially evolving currents and ocean density structure are needed to track the hydrocarbons outside the near-field region and to the coasts. Though the far-field experiences many of the processes discussed here, it also involves many other processes, especially those occurring at longer time scales. Given typical horizontal ocean current speeds, processes in the near field occur on the scale of seconds to hours, with about 1 day as the maximum residence time of petroleum fluids in the near field. Because of the short time scales involved, we ignore biological processes and focus on the physics and chemistry.

We have organized our review by focusing on the processes within the wellhead or the vent leading to the sea and then the jet and the formation of oil droplets and gas bubbles within a distance of tens of orifice diameters of the release. We then evaluate the migration of the plume to distances that can span vertically over the whole water depth and laterally to distances constrained by the decorrelation scale of the local ambient currents (up to $\approx$ 10 km). We also elucidate the chemical interaction of the hydrocarbons in the water column and the release of various hydrocarbon components into the environments.

2. Hydrodynamics Within the Conduit or the Well

It has been customary in the studies of multiphase jets and plumes to investigate the processes that occur downstream of the orifice (i.e., within the receiving water body). Examples include works that investigated bubble plumes (Milgram, 1983; Sun & Faeth, 1986), bubbly jets (i.e., bubbles released within a water jet)

(Martínez-Bazán et al., 1999a), and oil and gas releases in the field (Johansen, 2000, 2003) or in the laboratory (Neto et al., 2008; Socolofsky & Adams, 2002, 2003). These investigations shaped the general direction for investigating multiphase plume for the last two decades. However, during the investigation of the DWH spill, the role of the gas and liquid discharges within the pipe rose to prominence due to their implications on the estimation of the discharge and on the oil droplet size distribution (Boufadel et al., 2018).

When liquid and gas flow in a pipe, the flow regime depends greatly on their discharge values, as noted in various fields, such as nuclear engineering (Hewitt, 2012), polymer processing (Schmidt et al., 2008), gas condensate wells (Garber et al., 1998), volcanic eruption (Ulivieri et al., 2013), and oil and gas wells (Flores et al., 1997; Zhao et al., 2013). There are four major patterns of interest in vertical pipes: bubbly, slug (or plug), churn, annular, and dispersed flow (Figure 2a). The regimes can be estimated based on a flow "map," presented in Figure 2b as a function of the superficial velocity of liquid and gas (volume flow rate divided by the cross section area of the pipe). Bubbly flow occurs at a small gas flow and is characterized by the occurrence of gas bubbles dispersed within the liquid and both fluids moving upward. The type of the bubbles in this regime is governed by the values of the dimensionless numbers: Reynolds, Eotvos (Eo), and Morton (Bhaga & Weber, 1981). When the gas holdup (or content) is small (less than 5% per volume), the Eotvos number is less than 1.0 and bubbles tend to be spherical. As the gas fraction increases to around 20% to 30% (Azzopardi & Wren, 2004), some of the bubbles coalesce resulting in large structures which are no longer spherical. For these bubbles, the gravity forces around the bubble are larger than the surface tension force, leading to an Eotvos number larger than 1.0. When the bubble diameter increases to more than 50% of the pipe diameter, the flow could switch to slug flow (Chen & Brill, 1997), where the gas flow occurs through a train of bubbles each in the shape of a bullet (also known as a Taylor bubble) with liquid droplets and gas bubbles entrained behind the main bubbles. Liquid flow as a film along the walls remains upward. Also, the size (along the pipe) of the Taylor bubbles is no longer dependent on the Eotvos number but dependent on the overall hydrodynamics (i.e., discharges). As the gas flow increases to 50% per volume and if the pipe's diameter is larger than approximately 0.1 m (Kytömaa & Brennen, 1991), the pattern becomes that of churn flow (Orell & Rembrand, 1986), where the gas and liquid are no longer coflowing rather tumbling within the pipe. In this regime, one observes sporadic "flooding" of the pipe, which is a situation where a part of the liquid on the wall is transported upward while appearing highly disturbed, and another part flows downward (Govan et al., 1991; Parsi et al., 2015a). Churn flow results also in the manifestation of various instabilities at the gas-liquid interface. A further in the air flow rate results in the so-called annular flow where the gas migrates more or less steadily upward in the pipe with the liquid falling as a film at the walls and entrained as droplets in the gas phase (i.e., the liquid becomes dispersed in the gas). For high liquid velocity and only minimal gas velocity, the liquid droplets become more or less randomly distributed in the pipe, in a regime known as "dispersed" (Figure 2). The occurrence of various regimes depends also on the length of the conduit. In the experiments by Waltrich et al. (2013) in a 50 m long pipe (diameter 0.05 m), the flow progressed with the distance from slug to churn to annular.

Experimental techniques for characterizing these flows have been summarized by Montoya et al. (2016). A salient tool is the wire mesh sensor which is typically placed in the pipe's cross section to provide the spatio-temporal variability of the holdup. Flow maps using the superficial fluid velocity have been developed in various works (Hewitt et al., 1985; Wallis, 1969). But other works use the fluid's momentum (Hewitt & Roberts, 1969) or the Weber number (Parsi et al., 2015b). An important quantity that emerges is the dimensionless gas velocity, $U_g^*=u_{sg}\sqrt{\frac{\rho_g}{gd_{pipe}\left(\rho_l-\rho_g\right)}}$ where u_{sg} is the superficial velocity of gas, ρ_g is the gas density, ρ_l is the liquid density, g is gravity acceleration, and d_{pipe} is the pipe diameter. A value $U_g^* \geq 1.0$ indicates annular flow, while smaller values suggest churn flow. Models that reproduce the general behavior have been developed (e.g., Jayanti and Hewitt, 1992), and they were calibrated to data to provide, for example, the thickness of the liquid film and the size and rise speed of the Taylor bubble. However, there is no theoretical approach that is yet capable of capturing the impact of various parameters such as liquid viscosity (McNeil & Stuart, 2003), interfacial tension (IFT), pipe dimension, and large pressure. Using a wire mesh sensor to measure volume fractions in a vertical pipe with $d_{pipe} \approx 75$ mm, Parsi et al. (2015b) presented a map based on the superficial velocity (dimensional) of liquids and gas. They also used separately three liquid viscosities of 1, 10, and 40 centipoise (cp) and three liquid velocities below 1.0 m/s. The gas velocities varied

from 10 to 27 m/s. They found that for the same liquid superficial velocity, the gas fraction increases with the liquid viscosity. They attributed this behavior to a reduction of liquid waves and encapsulation of gas bubbles within the liquid. Their studies support prior studies (Da Hlaing et al., 2007) that the boundary between regimes become more diffuse with the increase in the viscosity, especially at low gas Reynolds number. The impact of interfacial tension on the general motion of the flow is negligible when the regime is churn as the large flooding waves are dominated by inertia (van Nimwegen et al., 2015). However, the interfacial tension is expected to play a major role in the formation of oil droplets in churn and annular flows (discussed next). Also, a large pipe diameter may suppress the formation of slug flow and cause the flow to switch directly from bubbly to churn flow; using water and air, Shah et al. (1982) reported that no slug flow occurs when the pipe diameter exceeded 0.10 m. Conversely, no churn flow would occur if the pipe diameter is smaller than a centimeter, and the flow regime would switch from bubbly to slug, as the diameter of the Taylor (gas) bubble would occupy more than 50% of the majority of the pipe cross section (i.e. a large fraction of the cross section).

As most of the investigations occurred under relatively low gas pressures (less than 100 m deep) (Waltrich et al., 2013), where the gas density ρ_g is around 1 kg/m^3 and the liquid density ρ_l is around 1000 kg/m^3, extrapolating churn flow "maps" to deepwater (say more than 1,000 m of water depth), such as the DWH, where ρ_g is around 120 kg/m^3 with live oil, where the density could be as low as 500 kg/m^3 (Gros et al., 2016, 2017; Zhao et al., 2015) is not evident.

Natural geophysical pathways for oil and gas releases are curvilinear (not straight), have variable cross sections, and possess rough walls, features that are likely to impact the flow regime in ways that have not been studied yet. Even constructed oil wells, such as the MC252, may contain internal protrusions (due partially to the presence of the blowup preventer) (Plume Calculation Team, 2010) that are likely to alter the flow regime (Boufadel et al., 2018). However, the occurrence of churn and slug flow regimes have been noted in pipes of various inclinations (Barnea, 1987) including horizontal (Navarro, 2005; Zhao et al., 2013), which is due to the large inertial forces in these flows. The impact of the discharge angle on the oil droplet size distribution (DSD) is not known. Thus, the existence of churn and slug flow regimes is common, whenever gas flow is not small. Large advances have been made in theoretical and computational methods of churn flow. However, the modeling is still limited by the accuracy of the interfacial momentum representation (Montoya et al., 2016), which renders the modeling via the Eulerian–Eulerian approaches extremely challenging due to the difficulty of assembling robust closure models for the deformable gas structures.

3. Jet Flow

Based on the work with miscible jets (e.g., water in water or air in air), studies have demonstrated the existence of a potential-flow cone that extends from the orifice to a few diameters, and the existence of a shear flow zone at the periphery of the jet where the ambient fluid is entrained into the jet (Bradshaw et al., 1964). Beyond the core, the turbulent axial velocity fluctuations in miscible jets were found to be more than double the radial ones near the orifice, and becoming equal at large distances (distance of 80 to 100 pipe diameters) due to momentum transfer (Wygnanski & Fiedler, 1969). Thus, turbulence is anisotropic initially and become isotropic at large distances from the orifice. The behavior of these plumes in strong cross flows have been well described (Fric & Roshko, 1994; Mahesh, 2013). Of importance is the formation of two counter-rotating vortices pairs that tend to trap the formed oil droplet, as discussed in section 5.2.

Various formulations have been developed to capture the hydrodynamics of miscible jets without cross flow based on experimental data, as summarized in Figure 3, which shows that the centerline velocity decreases with distance, x, as x^{-1}, and the energy dissipation rate is more or less constant for the first few diameters and then decreases according to x^{-4}, where x is vertical distance above the orifice (Hussein et al., 1994).

The length of the core (also known as the irrotational or potential core) is larger for immiscible fluids, such as oil in water, as observed in the experiments of Xue and Katz (2019), where the core length was around 6 diameters. This behavior seems to be related to the hydrophobicity of the oil to water, and thus, an oil jet tends to have more coherence than a miscible liquid jet. Gao et al. (2017) released oil from 2.4 mm orifice without and with dispersant and noted that the jet angle of the oil-only release was narrower than that of the jet angle of the oil with dispersant, whose angle was equal to that of miscible jets, 22° (Fischer

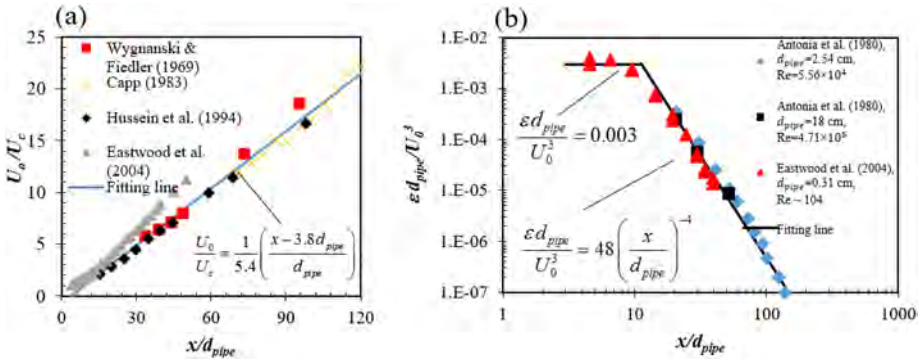

Figure 3. General behavior as function of distance, x normalized by the diameter of the pipe, d_{pipe}, of (a) the centerline velocity U_c as normalized by the centerline velocity at the orifice U_o and (b) the normalized energy dissipation rate (represents the energy dissipation rate). Taken from Zhao, Boufadel, et al. (2014) for miscible jets.

et al., 1979). They confirmed their observations using Reynolds-averaged Navier-Stokes (RANS) simulations using the software Fluent, and the module volume of fluid (VOF).

The presence of gas in a vertical pipe essentially eliminates the potential core due to the rapid horizontal excursion of gas bubbles. Boufadel et al. (2018) simulated churn flow in the DWH blowout and adopted a domain of 20 diameters in length, 10 within the riser (or pipe) and 10 downstream (i.e., above) the orifice. They used large eddy simulation (LES) and simulated the interface of the fluids using the VOF model, and they used the Smagorinsky subgrid model. Using VOF means that there is one momentum equation for both phases. They found that the Gaussian distribution captures well the ensemble radial variation of the axial velocity, consistent with works on miscible fluids and bubbly jets. However, the decrease of velocity with the radius was around 30% slower than that of miscible or bubbly jets. The radial distribution of the oil holdup in churn flow was broader than that resulting from an oil-only case (or bubbly flow). Also, the interface between the jet and the surrounding fluid was more irregular than that for bubbly flow, and it resulted in a larger water entrainment coefficient for churn flow (around 150% that of bubbly flow; see their Figure S12). Boufadel et al. (2018) reported also that the dimensionless energy dissipation rate $\frac{\varepsilon d_{pipe}}{U^3}$ (where ε is the energy dissipation rate, d_{pipe} is diameter of pipe, and U the superficial fluid velocity) within the pipe is five times larger for churn flow than for a bubbly or liquid flow. The difference in the dimensionless energy dissipation rate between churn and bubbly flows decreased to around double within 4 diameters from the orifice. Thus, due to its larger energy dissipation rate, churn flow is likely to result in smaller oil droplets in comparison to oil only or bubbly flow.

4. Oil Droplet Size Distribution (DSD)

The oil DSD resulting from a jet determines, to a large extent, the trajectory of the released oil; large droplets (e.g., >500 microns) migrate rapidly (minutes to hours) to the surface (Zhao et al., 2015) while small droplets could be transported horizontally by currents (Figure 1a) or by the intrusion (Figure 1b) (Gros et al., 2017; Wang & Adams, 2016; National Academies of Sciences Engineering Medicine (NASEM), 2019). In addition, oil dissolution (Stevens et al., 2015) and/or biodegradation (Prince et al., 2017; Socolofsky et al., 2019) increase with the oil-water surface area, and thus, a decrease in droplet diameter (i.e., an increase in the surface area per unit volume of oil) would promote these processes.

There is no experimental work providing the oil DSD based on the release of two phases (oil and gas) into a third phase (namely water). Socolofsky and Adams (2002) released such plumes in laboratory setups, but they were focused on plume behavior and, thus, did not provide the oil DSD (or the gas bubble size distribution). For this reason, we will present experimental works that addressed the release of oil in water. Still, the number of these works is small in comparison to that of experimental and numerical works on the DSD of hydrocarbons released in gas, obtained mostly from the field of engine combustion.

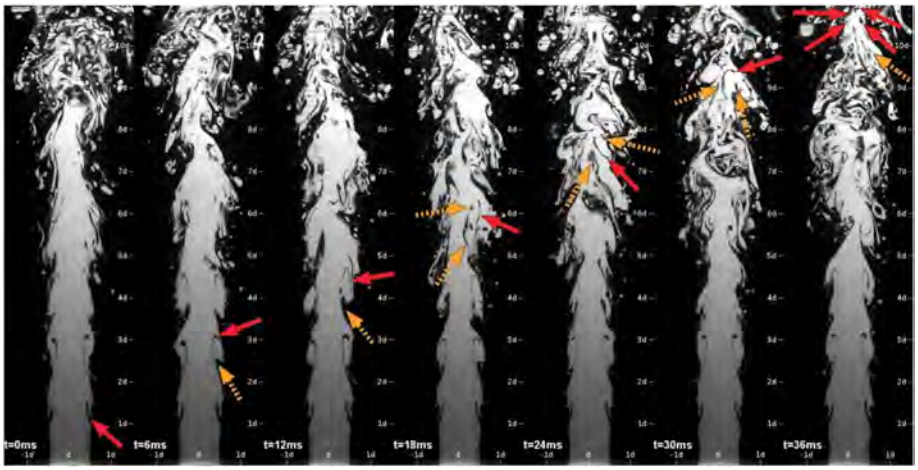

Figure 4. A time sequence showing processes leading to compound droplet formation at Re = 1,358. The symbol "d" is the pipe diameter, which was 1.0 cm. Arrows of the same color (red or orange) and shape (solid or dashed) follow the same water ligament in the frames separated by 6 ms. Taken from Xue and Katz (2019).

In an oil-only release, the oil DSD is the result of shear at the edge of the oil jet, which forms Kelvin-Helmholtz instabilities (Figure 4) that generate ligaments and droplets at the edge of the plume that get entrained subsequently into the plume (Figure 4) due to the jet momentum and buoyancy. Turbulence within the plume causes these ligaments and droplets to break up further. Major insights on the breakup of oil droplets in turbulent flow were introduced by Hinze (1955), discussed next.

Hinze (1955) considered that the destructive forces are due to the dynamic pressure and that the resisting force is due to the interfacial tension between oil and water. From that he concluded that the largest diameter that can survive in turbulence (approximated by the d_{95}) can be estimated by setting the Weber number $W_e = \frac{\rho_c u'^2 d_{95}}{\sigma}$ (where ρ_c is the density of the continuous fluid (water herein), u' is the root-mean-square turbulence velocity, and σ is the oil-water interfacial tension coefficient) to a critical value W_{ec}. For isotropic turbulence, W_{ec} was found to be around 1.17. However, different critical values occur in other flows (e.g., hyperbolic). The turbulence velocity was estimated by assuming isotropic turbulence at the scale of the droplet, u'^2 scales with $\varepsilon^{2/3} d^{2/3}$, and thus, knowledge of the average energy dissipation rate, oil-water interfacial tension, and W_{ec} would provide d_{95}. Hinze (1955) addressed also the situations where the viscosity of the droplet resists breakup and introduced a viscosity group, $V_{i,G} = \frac{\mu_d}{\sqrt{\rho_d \sigma d_{95,v}}}$ (where ρ_d and μ_d are the density and dynamic viscosity of the dispersed phase and $d_{95,v}$ is the largest diameter while accounting for the viscosity of the droplets). Using dimensional analysis, he argued that a Weber number that accounts for viscosity W_{ev} would be related to W_{ec} and $V_{i,G}$ through $W_{ev} = W_{ec}(1+\varphi V_{i,G})$ where $\varphi \to 0$ as $V_{i,G} \to 0$. These concepts were expanded on in the 1980s (Calabrese et al., 1986; Wang & Calabrese, 1986) for dealing with high viscosity oils in chemical reactors, where the dynamic viscosity reached 10,000 cp (the water dynamic viscosity is ≈ 1.0 cp). They obtained the DSD after 2 hr of mixing and found that even at such high viscosities, the contribution of the interfacial tension remains important (small but not negligible). The breakup of oil droplets and ligaments within the jet is likely to occur due to the dynamic pressure resulting from turbulence (Hinze, 1955) and capillary instabilities of elongated threads. The breakup of droplets due to shear below the Kolmogorov scale could be considerable for oil jets with large viscosity, where the Kolmogorov scale (based on oil) $\eta_o = \left(\nu_o^3/\varepsilon\right)^{1/4}$ is large. But large viscosity oils do not flow as easily, and thus, their discharge velocity is likely to be relatively small.

The formation of droplet from jets can be well characterized using the Ohnesorge versus Reynolds diagram (Figure 5) (Masutani & Adams, 2001). The Ohnesorge number is defined as $Oh = We^{1/2}\mathrm{Re}^{-1}$ and, thus, combines the viscosity of the oil droplet with the interfacial tension forces. In Figure 5, the zone to the right of the

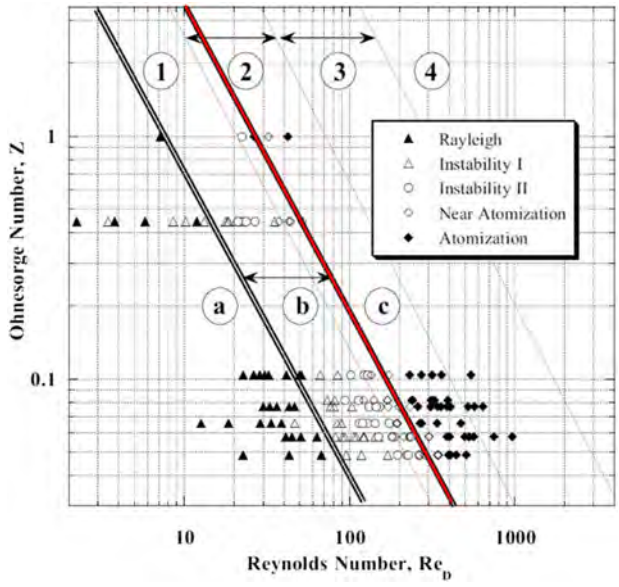

Figure 5. Jet breakup instability regimes. Data points were obtained by oil injection into water by Masutani and Adams (2001). The double lines are the inferred boundaries of three breakup regimes denoted as (a) Rayleigh, (b) Types I and II, and (c) atomization. Solid lines are the boundaries established in previous investigations of liquid jets discharging into a gas where 1 is the Rayleigh regime, 4 is the atomization regime, and 2 and 3 correspond, respectively, to the first and second wind-induced breakups. Taken from Masutani and Adams (2001).

red line is within the atomization regime, where the breakup of oil droplets is due to turbulence, which is the interest of this paper.

The size of the oil droplets decreases with the application of dispersants, which reduce the oil water IFT. Dispersants are manufactured chemicals that include a mixture of anionic and nonionic surfactants and a solvent (National Academies of Sciences Engineering Medicine (NASEM), 2019). The surfactant molecules have a lipophilic tail that sticks to the oil and a hydrophilic head that orients to be in water. Historically, dispersants were designed to be applied on oil slicks (i.e., on the water surface) to dilute them into the water column, as the goal has been to prevent the oil from reaching the shorelines where it can cause a major impact to ecology and economy (National Research Council of the National Academies, 2013) and/or it can persist for decades (Li & Boufadel, 2010; Reddy et al., 2002). The DWH was the first time that a dispersant was applied at depth. The reduction of the overall droplet size due to dispersant application has been noted in various works (Brandvik et al., 2013; Li et al., 2008a, 2008b; Pan et al., 2016). Within the context of Figure 5, reducing the IFT increases the Oh number and, thus, causes further atomization at the same *Re* value.

The addition of dispersant engenders the mechanism of "tip streaming," which generates micron-sized droplets (De Bruijn, 1993; Eggleton et al., 2001). However, tip streaming, whereby the oil "slough off" of the droplets in microthreads, has been gaining attention. This occurs due to the migration of the dispersant on the oil droplet to the leeward side, causing the accumulation of the dispersant at specific locations on the droplet wake (or leeward side), which causes a significant decrease in the oil-water interfacial area (Gopalan & Katz, 2010). These threads later undergo a sinuous wave instability and break up into tiny droplets a few micrometers in diameter. Tseng and Prosperetti (2015) used detailed mathematical derivations and demonstrated that the dispersant would accumulate in the zones of zero vorticity on the oil droplet, labelled as stagnation zones or "points." Tip streaming explains the presence of a micron-sized mode within bimodal DSDs in cases where dispersants are applied to oil on waves (Li et al., 2008a; Mazzitelli & Lohse, 2009) and to oil jets (Murphy et al., 2016; Zhao et al., 2017).

4.1. Oil DSD Experiments

The DeepSpill experiment (Johansen et al., 2001) remains one of the major experiments of hydrocarbon release at the field scale. It involved injection of nitrogen gas and seawater, natural gas and marine diesel, natural gas and crude oil, and natural gas and seawater. The ocean conditions during the experiment had high currents and low stratification. Nonetheless, the plume of oil, gas, and entrained seawater trapped at heights less than 200 m above the sea floor, and the majority of the oil droplet transport was accounted for by passive, Lagrangian transport with the mean ocean currents and droplet slip velocity. The oil droplet size distribution for some of the experiments was measured by a camera on a remotely operated vehicle (ROV), and the majority of the measurements were of acoustic backscatter from the bubbles recorded by an onboard echo sounder on the observation vessel. Ocean currents were measured by an upward looking acoustic Doppler current profiler moored on the seafloor near the discharge point. Until the DWH accident, this data set comprised the only ocean-scale observations of a multiphase plume relevant to the dynamics of a subsea blowout. The maximum oil droplet size was around 14 mm, but there was a variability in the oil DSD, due to the logistical constraints in conducting such a challenging experiment.

Masutani and Adams (2001) conducted experiments of oil release from 2.0 and 5.0 mm orifices at various flow rates at Reynolds number of ≈100 to 3,000. They measured the oil droplet size using phase Doppler particle analyzer and reported droplets up to 4 mm in size. They were not able to measure larger droplets due to equipment limitations. Brandvik et al. (2013) released oil from 1.0 and 2.0 mm orifices into a 6.0 m vertical (3.0 m diameter) tank. They also applied dispersant into the jet at a dispersant to oil ratio (DOR) of 1:100 and

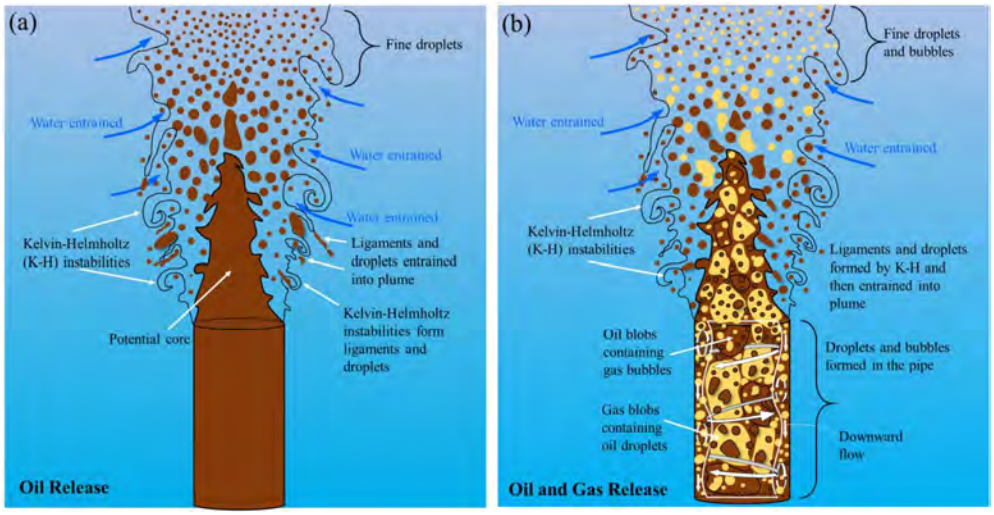

Figure 6. Jets of fluids into water. (a) For oil only release, Kelvin-Helmholtz (KH) instabilities generate ligaments and droplets that get entrained into plume and subsequently disintegrate due to turbulence within the plume. An intact core of oil (under potential flow conditions) exists within a few diameters of the orifice. (b) For oil and gas release, ligaments and droplets emerge also from the pipe, and they combine with those formed due to KH; a potential core of oil and/or gas does not exist.

up to 1:20, which reduced the oil-water interfacial tension, resulting in smaller droplets. They measured the oil DSD using the instrument LISST (Laser in Situ Scattering and Transmissiometry, from Sequoia) (see Zhao et al., 2018, and reference therein). Murphy et al. (2016) released crude oil from a 4.0 mm vertical orifice in a crossflow (by towing the release). Their largest Reynolds number was 1,000, and they applied dispersants at the DORs of 1:100 and 1:25. They measured the oil DSD using holography and found the d_{50} to be around 700 microns for oil only and down to 230 microns for DOR at 1:25. They observed a multimodal distribution for the number-based DSD. Zhao et al. (2017) released oil horizontally from a 2.4 mm orifice and monitored the DSD using LISST. They used the LISST for measurement and found the droplets to be smaller than 400 microns. The exit velocity was large (around 13 m/s) and the Reynolds number was around 2,000. Xue and Katz (2019) used an index matching method that allowed them to measure the oil DSD in a plane crossing the center axis of plumes emanating from a 10 mm diameter nozzle at Reynolds numbers varying from 600 to 2,400. The nozzle that they used produced a top-hat (i.e., radially uniform) velocity profile at the orifice. They observed composite droplets where oil engulfs water containing smaller oil droplets (Figure 4). They also found that the large droplets were deformed (elongated), while the small droplets were spherical, suggesting a sheltering from the jet shear. They also found that the diameter of the large droplets decreases with the jet Reynolds number, but the diameter of the small droplets was unaffected by the jet Reynolds number.

4.2. Droplet Size Distribution From a Churn Flow Blowout

For an oil-only plume, Kelvin-Helmholtz instabilities due to shear around the jet (Figures 4 and 6a) are the major mechanism for forming droplets. But for churn flow, an additional source exist which is the oil droplets and blobs (large oil agglomeration) present in the pipe and emanating from the orifice (Figure 6b). As the DSD in the plume depends on the size of oil droplets at the orifice, it is important to understand the DSD within the pipe. The size of the median droplet entrained in gas flow has been the subject of various investigations (Ishii & Mishima, 1989; Kataoka et al., 1983; Wang et al., 2013). The mechanism of droplet formation in these systems (i.e., churn) is due to roll off from the liquid film due to shear rather than fragmentation within the gas stream. This was indirectly confirmed by the fact that the size of droplets due to fragmentation in gas flow (i.e., based on the dynamic pressure of gas and/or Rayleigh instability) is larger than those observed in churn flow system within the gas. Based on investigations of churn and annular flow at liquid Reynolds number reaching 3,000, Kataoka et al. (1983) reported that the droplet size in annular flow varied from 10^{-5} to 10^{-3} m. Kataoka et al. (1983) proposed that the Weber number of entrained

droplets of size $d_{E,m}$ (taken herein as the median volume diameter) is related to fluid and hydrodynamic properties in the pipe through:

$$W_{e,d}=\frac{d_{E,m}\rho_g j_g^2}{\sigma}=0.01\,R_{e,g}^{2/3}\left(\frac{\rho_g}{\rho_l}\right)^{-1/3}\left(\frac{\mu_g}{\mu_l}\right)^{2/3} \quad (1)$$

where j_g is the gas volumetric flux (also known as superficial velocity) and $R_{e,g}=\frac{\rho_g d_{pipe} j_g}{\mu_g}$ is the gas Reynold number. This form of the Weber number was confirmed to be valid for predicting droplet sizes from churn flow (Wang et al., 2013). The fraction of entrained liquid in the form of droplets within the gas phase was reported to be around 0.2 and to reach up to 0.6 for churn flow (Barbosa et al., 2002; Ishii & Mishima, 1989; Wang et al., 2013)

As an illustration of Equation 1, the median volume diameter, $d_{E,m}$, for the DWH release would be on the order of 4.0 mm, based on the liquid oil and gas properties at the release point used by either Zhao et al. (2015) or Gros et al. (2017). The former used empirical relations developed by oil reservoir engineers, and the latter used a detailed thermodynamic model. However, predicting the fraction of entrained liquid for the DWH is challenging, because the entrainment fraction reported above (20% to 60%) are based on mostly air-water systems at pressures less than 30 m of water. Thus, extrapolating these results to high pressure, where the gas density is 120 kg/m^3 (i.e., $\approx$ 100 times of gas density used in the experiments), may not be acceptable.

The oil DSD depends also on the coalescence of oil droplets which is similar to breakup in a sense that it depends on the mixing energy. However, coalescence depends also on (actually increases with) the oil holdup (or oil concentration), which determines the chance of two droplets colliding. Mixing energy impacts both the collision frequency and collision efficiency of droplets. A system with a large mixing energy (large energy dissipation rate) would result in a large collision frequency, but if the droplets do not stay in contact long enough to coalesce, the coalescence efficiency would be low (Liao & Lucas, 2010; Tsouris & Tavlarides, 1994). The collision frequency also increases with the holdup (i.e., more droplets per unit volume). Based on studies in reactor, coalescence was found to be important in systems with oil holdup larger than 30% per volume. The average oil holdup in a jet's cross section depends on the volumetric discharges of oil and gas from the orifice and the water volume that was entrained between the orifice and the cross section. Thus, it is expected that the oil holdup from a churn flow (where the gas flow is large) is smaller than that from a bubbly flow. However, in terms of oil droplet coalescence, the spatial distribution of oil, water, and gas at the micron scale within the cross section plays a more important role, because it is the neighborhood of the droplet that determines its coalescence with other droplets. Some models of oil droplet formation accounted for the presence of gas through a reduction in the cross section area of the orifice (Johansen et al., 2013; Li et al., 2017; Zhao, Boufadel, et al., 2014). However, such an approach is likely to overestimate the extent of coalescence and, thus, overestimate the size of the oil droplets. Nevertheless, in comparison with bubbly jets, the "sputtering" behavior of churn flow jets and the large entrainment of water from them are likely to result in little coalescence of the oil droplets.

Although droplet formation through breakup is likely to be highest near the orifice, three processes suggest that the breakup is likely to occur within up to 100 pipe diameters from the orifice. The first process is coalescence, which depends greatly on the oil holdup (as discussed above); coalescence is largest near the orifice where the oil holdup is large, and thus, an oil droplet does not exist without the presence of water or gas around it regardless of the mixing energy. The second process relates to the heterogeneous nature of turbulence, which results in large local velocity fluctuations downstream of the orifice. Martínez-Bazán et al. (1999b) released bubbles in a water jet and observed that the breakup of the bubbles continued until around 40 diameters from the orifice. In fact, because turbulence is inhomogeneous, all works on the breakup of oil in systems (reactors, jets, and waves) relied on representing the breakup through a breakage frequency $g(d)$ derived from fundamental principles with constants obtained by fitting to data (Aiyer et al., 2019; Tsouris & Tavlarides, 1994; Zhao, Boufadel, et al., 2014). The third mechanism that favors additional breakup at large distances from the orifice relates to the buoyancy of plumes from large orifices, such as the DWH, where a relatively large rise velocity and energy dissipation rate would persist for 100s of diameters from the jet (Zhao et al., 2015).

4.3. Model to Predict the Evolving Oil Droplet and Gas Bubble Size Distributions

Johansen et al. (2013) extended the concepts introduced by Hinze (1955), Calabrese et al. (1986), and Wand and Calabrese (1986) to predict the size of oil droplets from jets. They postulated that for a release of oil at a velocity U, one has $W_{e,v} = W_e[1+BV_i(d_{50}/d_{pipe})^{1/3}]^{-1}$, where B is a constant, and d_{50} is the volume median diameter, W_e is the Weber number, defined as a function of the jet diameter and velocity, $W_e = \frac{\rho_d U^2 d_{pipe}}{\sigma}$ and $W_{e,v}$ is modified Weber number that accounts for viscous forces. The term V_i is the viscosity number given by $V_i = \frac{W_e}{R_e} = \frac{\mu_d U}{\sigma}$; the Reynolds number, $R_e = \frac{\rho_d U d_{pipe}}{\mu_d}$; a related dimensionless number to V_i is the Ohnesorge number $Oh = W_e^{1/2} R_e^{-1} = \frac{\mu_d}{(\rho_d \sigma d_{pipe})^{1/2}}$. Johansen et al. (2013) hypothesized that the d_{50} from a vertical jet can be predicted based on the size of the orifice and modified Weber number as follows:

$$\frac{d_{50}}{d_{pipe}} = AW_{e,v}^{-3/5} = AW_e^{-3/5}\left[1 + BV_i\left(d_{50}/d_{pipe}\right)^{1/3}\right]^{3/5} \tag{2}$$

In the presence of gas, the velocity U becomes the "effective" velocity computed by assuming constriction due to gas. By fitting to droplet data in vertical jets from millimeter size orifices without and with dispersant, Brandvik et al. (2013) found $A = 15$ and $B = 0.8$. In a subsequent work, the group estimated $A = 24$ and $B = 0.08$ (Brandvik et al., 2014). Johansen et al. (2013) considered that the full DSD can be predicted by assuming a lognormal distribution for cases without dispersant and by Rossin-Ramler (or Weibul) distribution for cases with dispersant. The variances of these distributions would be obtained based on experiments.

The role of the viscosity number in Equation 2 becomes important when dispersants are used resulting in small IFT, which result in a very large viscosity number V_i, and thus, the bracket term becomes large. In these situations, neglecting the viscosity of the oil would underestimate the d_{50}. The approach of Johansen et al. (2013) follows that of Sleicher (1962) who obtained the maximum oil droplet size in turbulent water flow in pipes using the correlations of Hinze (1955).

Li et al. (2017) argued that Equation 2 results in droplet sizes increasing with the diameter of the pipe and, thus, could overestimate the size of droplets from large orifices as the droplets could then become larger than the maximum stable droplet, d_{max}, obtained based on the Rayleigh criterion for stability of an individual droplet (Grace et al., 1978), which gives

$$d_{max} = 4\left[\frac{\sigma}{(\rho_c - \rho_d)g}\right]^{1/2} \tag{3}$$

Based on the arguments above, they proposed the following correlation:

$$\frac{d_{50}}{d_{pipe}} = 14.05 * W_{e,Li}^{-0.518}(1 + 10 * Oh_{Li})^{0.46} \tag{4}$$

where d_{pipe} is the orifice diameter or d_{max} (Equation 3) whichever is smaller. The Weber number used in Li et al. (2017) is defined as $W_{e,c} = \frac{\rho_c U^2 D}{\sigma}$ and is thus based on the continuous phase (i.e., water) density. In Equation 4, the Ohnesorge number is defined as follows: $Oh_{Li} = \frac{\mu_d}{(\rho_d \sigma d_{pipe})^{1/2}}$. One notes the similarity between Equations 2 and 4 in terms of the exponents of the Weber number (−0.52 vs. −0.6) and the coefficients multiplying the Weber number (14.05 versus $A = 15$) . For situations with dead oil (i.e., density close to that of water) and orifices smaller than d_{max}, the two equations give essentially the same results. Similar to the approach of Johansen et al. (2013), Li et al. (2017) assume the oil DSD to be fit by the lognormal distribution, the variance of which is estimated from data. In addition, the Li et al. (2017) correlation requires that the oil properties used in Equation 4 to be those of dead oil (i.e., the oil under atmospheric conditions), and thus, there does not seem to be a means to account for the density of live oil at different depths.

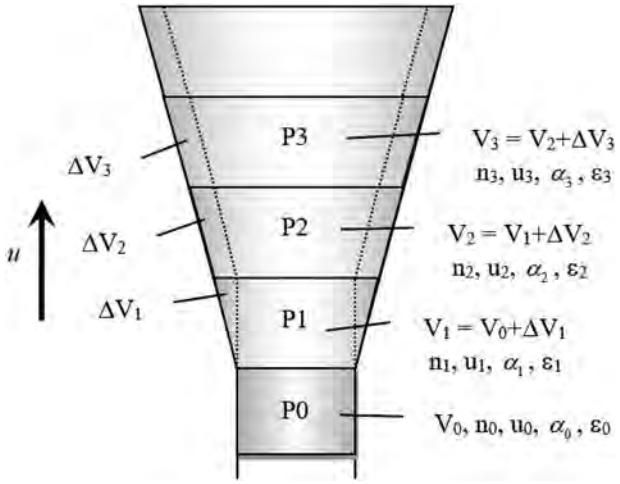

Figure 7. Illustration of the fluid parcel moving along the jet trajectory. The terms V, n, u,α andε represent the volume, number concentration of droplets, velocity, holdup, and energy dissipation rate, respectively. Taken from Zhao, Boufadel, et al. (2014).

Both correlation models are expedient for obtaining the d_{50}. However, they do not provide a physically based approach for obtaining the oil DSD. This could become an issue when the d_{50} obtained from Equation 2 or Equation 4 is close to $d_{\max}$, and thus, the DSD would have to be truncated above $d_{\max}$. For example, to maintain the d_{50} given by Equation 4, Dissanayake, Crowley, et al. (2018) used a truncated distribution at $d_{\max}$, where all diameters larger than $d_{\max}$ were placed at $d_{\max}$. In addition, the formation of micron-sized droplets due to tip streaming cannot be captured.

The VDROP-J model is a population model for predicting the oil droplet size distribution from multiphase jets (Zhao, Boufadel, et al., 2014). It combines the droplet population model VDROP (Zhao, Torlapati, et al., 2014) that applies to a control volume, with correlations for jet/plume properties in the near field (within 100 diameters from the orifice). The population model VDROP accounts for the simultaneous breakup and coalescence of oil droplets. Breakage is assumed due to the dynamic pressure resulting from isotropic turbulence and is accounted for using a breakage frequency, $g(d_i)$ given by $g(d_i) = K_b \int_{n_e} S_{ed}\left(u_e^2 + u_d^2\right)^{1/2} BE(d_i, d_e, t) dn_e$ where S_{ed} is the cross section area between a droplet of size d_i and an eddy of size d_e. The terms u_e and u_d are the speeds of an eddy and a droplet, respectively. The term BE is the breakage efficiency given by $BE(d_i, d_e, t) = \exp\left[-\frac{1}{c_1}\left(\frac{E_c + E_v}{e}\right)\right]$ where E_c and E_v are the resistance energies to breakup due to surface tension and droplet viscosity, respectively; e is the energy of an eddy and "c_1" is an empirical constant of order 1.0. The term K_b is an empirical constant discussed below. Similar to various population models, VDROP assumes that only eddies of comparable and smaller size than the droplet break it, while eddies larger than the droplet would advect it (Prince & Blanch, 1990; Tsouris & Tavlarides, 1994). This is obviously a mathematical convenience as eddies a few folds larger than the droplets are still expected to break it. Even larger eddies could break up a droplet in what is known as viscous turbulence. Studies (Eastwood et al., 2004; Martínez-Bazán et al., 1999a) argued for an approach where all the eddies can break the bubble and obtained a breakage frequency using all the eddies in the domain. Their approach resulted in a breakage frequency that decreases with the bubble diameter, which means that the probability of breakup of large bubbles is smaller than that of smaller bubbles, which is not expected.

In the vast majority of works on population models, the resistance to breakup was assumed to occur due to interfacial tension (i.e., the Weber number), the exception is the VDROP-J model, which includes the viscous resistance formulation (the letter V in VDROP refers to viscosity) based on the works of Calabrese et al. (1986) and Baldyga and Podgórska (1998). Baldyga and Podgórska (1998) accounted for the role of droplet viscosity through an elongation time prebreakup of droplet and assumed that droplets break up when their length is equal to double their initial diameter. They also considered the impact of intermittency, that is, the occurrence of rare large pulses of the energy dissipation rate. Using a multifractal representation of turbulence (Frisch & Parisi, 1985), they argued that given sufficient time, the rare energy dissipation pulses would interact with the whole droplet population and reduce the droplet size even further. In this regard, they viewed the commonly measured DSDs to be quasi-stable that would converge to the asymptotically stable DSD given sufficient mixing time. The model of Baldygha and Podgorska considered that only eddies of equal size to the droplet would break it, but they integrated the dynamic pressure resulting from the whole multifractal spectrum (Anselmet et al., 1984; Meneveau & Sreenivasan, 1987) and applied it to the droplets of that size. Within VDROP-J (and VDROP), the coalescence of droplets is captured using a coalescence frequency, $h(d_i, d_j)$ (Luo & Svendsen, 1996; Narsimhan et al., 1979; Tsouris & Tavlarides, 1994), where d_i and d_j are any 2 diameters.

The correlations used within VDROP-J model to move conceptually the control volume downstream along the jet centerline were obtained based on the hydrodynamics of miscible jets, and they include the change

along the centerline jet velocity (Figure 3a), flow rate (due to entrainment of ambient liquid), and jet energy dissipation rate (Figure 3b). The oil mass is moved downstream of the jet (Figure 7) by advection (i.e., by the centerline velocity), where the model VDROP is solved using the upstream DSD and the local properties (oil holdup and energy dissipation rate) as input to obtain the DSD at the current distance x/d_{pipe}. The VDROP-J model was validated in a two-step approach. The first consisted of comparing the VDROP model to data from reactors at transient and steady state (Zhao, Torlapati, et al., 2014) and the second after combining the VDROP model with the jet/plume correlation relations (Zhao, Boufadel, et al., 2014).

The impact of dispersant on the overall oil DSD has been modeled by updating the oil water IFT using a value based on laboratory experiments with the predicted dispersant to oil ratio. Micron-sized droplets resulting from tip streaming cannot be captured by correlations of Equation 2 or Equation 4. Using VDROP-J, Zhao et al. (2017) introduced a module within VDROP-J to simulate tip streaming using a "mass transfer" formulation; the decrease of the total mass of oil droplets with diameter d_i, M_{di} was given by $\frac{\mathrm{dM}_{di}}{\mathrm{dt}} = -k_{\mathrm{tip}} J_0$, where J_0 is the mass flow rate leaving the mass M_{di} and k_{tip} is a mass transfer coefficient (dimensionless) that depends on the hydrodynamics around the droplet and the interfacial tension in the jet. The mass that sloughs off the droplet, was assumed to be Gaussian centered at 2.0 microns.

The decrease in pressure from live oil could play an important role if the pressure drop is rapid. Experimental works indicate that a decrease in pressure by 3 to 10 bars across a millimeter size orifice could cause the disintegration of a live oil droplet (Malone et al., 2018). Other experiments along the same vein were conducted by Pesch et al. (2020) who showed the droplet increasing in size due to the expansion of the gas within it. These experiments were conducted from small orifices under laminar conditions. The role of gas expansion under turbulent conditions is not known, as the dynamic pressure of turbulence would cause the live oil droplets to break during expansion.

5. Plume and Multiphase Plume Dynamics

The concept of a buoyant plume originated with studies of cloud physics by Morton et al. (1956), who proposed the integral approach to the governing equations of the plume evolution. This approach solves for the cross sectionally averaged quantities of volume flux, momentum flux, and buoyancy flux, and formulation of the governing equations relies on the assumption of self-similarity: Horizontal profiles of velocity and concentration have the same shape at all heights in the plume, and distance along the plume is the only relevant geometric length scale. A key success of these early models was in their turbulence closure. In a homogeneous, unbounded domain, jets and plumes spread with a constant spreading rate and are strictly self-similar. Morton et al. (1956) showed that this is also equivalent to a constant entrainment coefficient, α, that relates the velocity of the inward flow, caused by the entrainment of ambient fluid, to a characteristic, axial velocity in the plume. This more general turbulence closure scheme allows integral models to be applied in cases where self-similarity breaks down, as in the atmosphere and oceans when density stratification is present. The ambient stratification imposes a second geometric length scale on the problem, the height of the intrusion layer, violating the requirements for self-similarity. Morton et al. (1956) demonstrated that, nonetheless, entrainment models based on self-similarity could predict plume dynamics through to the intrusion formation even in stratified environments; see also a review of the entrainment hypothesis in Turner (1986). These early concepts have grown into a whole field of study for continuous-phase buoyant jets and plumes (Jirka, 2004; Jirka & Domeker, 1991; Lee & Cheung, 1990; Lee & Chu, 2003; Lee & Jirka, 1981; Whitehead et al., 1996; Woods, 2010).

Shortly after introduction of the integral model approach to jets and plumes, models were adapted to multiphase plumes (see also section 7), involving water as the ambient reservoir and bubbles or droplets as the dispersed phase. Bubble plumes were of interest for their natural occurrence in nature and for engineering applications in reservoir aeration, bubble breakwaters in harbors, bubble currents to contain oil slicks in the ocean, and in chemical engineering mixing processes (Milgram, 1983; Socolofsky & Rehmann, 2013). Kobus (1969) measured entrainment in bubble plumes, and the first integral models developed for bubble plumes using the entrainment hypothesis were by Cederwall and Ditmars (1970). These models recognized that buoyancy moves with the rise velocity of the dispersed phase; hence, the buoyancy transport in the momentum conservation equation was formulated with the mean plume velocity and an added bubble

slip velocity. Because entrainment is quite large, these bubble plumes were assumed to be dilute so that the void fraction could be ignored in the conservation of mass. Hence, integral models of multiphase plumes resemble single-phase models with an added slip velocity accounting for the transport velocity of the dispersed phase in the momentum conservation only.

From the first observations in bubble plumes (Cederwall & Ditmars, 1970; Kobus, 1969), it was recognized that the multiphase plumes were not strictly self-similar. This was evident by the fact that in a uniform ambient reservoir bubble plumes do not spread out with a constant spreading rate. Milgram (1983) proposed the first comprehensive integral model of a multiphase bubble plume and collected a wealth of observation data from the literature for model validation. He accounted for the nonuniform spreading rate through a variable entrainment coefficient, which he computed from laboratory observations and which he correlated with a type of bubble Froude number F_B, given by

$F_B = \chi^{2/5}\frac{L_B}{L_D}$ where χ is the centerline void fraction, L_B is a measure of the mixing distance of bubble motion represented as $L_B = \left[Q_p^2/(g\chi^2)\right]^{1/5}$, and L_D is a characteristic distance between bubbles represented as $L_D = [\sigma/(g(\rho - \rho_p))]^{1/2}/\chi^{1/3}$; Q_p is the gas flow rate at the source, g is the acceleration of gravity, σ is the interfacial tension of gas-water, ρ is the water density, and ρ_p is the gas bubble density at the release. Later, the mathematical reason for the lack of self-similarity was recognized by Bombardelli et al. (2007). Because the dispersed phase introduces a new velocity scale (i.e., the slip velocity), a second geometric length scale emerges even in a homogeneous environment. This scale, $L_{dispersed}$, combines the buoyancy flux of the plume B_f with the slip velocity u_s in the form of $L_{dispersed} = B_f/u_s^3 = g\left(\left(\rho - \rho_p\right)/\rho\right)Q_p/u_s^3$. Hence, as bubbles slip through the plume, they exert their influence over a length proportional to L_D. Despite the lack of strict self-similarity in bubble plumes, like single-phase plumes in ambient stratification, integral models based on the entrainment hypothesis still performed well in predicting their time-averaged, bulk dynamics.

Integral models of multiphase plumes were extended to density-stratified ambient environments for application to aeration in stratified reservoirs (Asaeda & Imberger, 1993; Wüest et al., 1992) and to understand the dynamics of possible subsea oil well blowouts in deepwater (McDougall, 1978). As explained in section 1, stratification gives rise to intrusion formation, and for multiphase plumes, the dispersed phase may not follow the entrained water into the intrusion. Both Asaeda and Imberger (1993) and McDougall (1978) performed laboratory experiments for bubble plumes in stratification and proposed integral models with an inner plume of bubbles and entrained water and an outer plume of water only that contributed to the intrusion formation. The algorithm to detrain inner plume water and feed the outer plume was further refined by Crounse et al. (2007). These double-plume integral models would effectively predict the intrusion height of the detraining water and, given the necessary initial conditions at the top of the peeling region, could predict multiple sequences of intrusion layers as the bubbles continued to form new plumes above each intrusion layer.

Asaeda and Imberger (1993) and McDougall (1978) proposed different combinations of the governing parameters controlling the plume dynamics. In both cases, because they were interested in finite-depth reservoirs, these parameters included the water depth H and the buoyancy frequency of the ambient stratification N, given by $N = \left[\frac{-g}{\rho}\frac{\partial \rho}{\partial z}\right]^{1/2}$ where z is the vertical coordinate, positive upward. In their analysis, a key parameter was the ratio of the water depth to the characteristics length scale of the intrusions $L_T = \left[\frac{B}{N^3}\right]^{1/4}$. Socolofsky and Adams (2002, 2003, 2005) performed similar experiments for bubble plumes in density stratification and considered deep water, where the trap height would be much less than the water depth, hence ignoring the water depth, H. They proposed an alternative governing parameter in bubble plumes, which can be viewed as a ratio of L_T/L_D, in the form of the velocity ratio $U_N = \frac{u_s}{(BN)^{1/4}}$. Using this scaling, Socolofsky and Adams (2003, 2005) correlated observations of trap height, peel height, and peeling flux expressed in nondimensional form with U_N. When using these data for model validation, Chu and Prosperetti (2017) point out that the trap height is fundamentally different from the neutral level

predicted by integral models and suggest approaches to make proper model-data comparison. Chu and Prosperetti (2019) further point out the importance at the field scale of dissolution and pressure expansion during plume rise on plume structure for droplet and bubble plumes. These effects vary with depth and dispersed phase but generally depend on the dissolution rate compared to the rise time to the neutral level, the effect of the dissolved material on the density of the entrained ambient water, and on the ratio of the dispersed phase slip velocity to a characteristic plume fluid velocity. Integral models that include these effects (e.g., dissolution, pressure expansion, and multiple phases) are discussed in more detail in section 7.

Socolofsky and Adams (2002) considered the effects of crossflow on bubble, droplet, and multiphase plumes. They showed that water entrained near the source of the plume will rise some characteristic distance L_S, but if the slip velocity of the dispersed phase is large enough, the continuous phase will separate from the dispersed phase and enter the wake of the plume. They also showed that faster-rising bubbles or droplets will be found at the upstream side of the plume, whereas smaller bubble or droplets will be swept to the downstream side of the plume. This process was called fractionation. Taken together, these observations demonstrated that multiphase plumes differ from single-phase plume by the independence of the dispersed phase particles: Their rise velocity allows them to follow a different path from the entrained continuous-phase fluid, and this can result in multiple intrusions forming in stratified conditions and separation of the entrained water to the wake of the bubble column in a crossflow.

The balance between momentum of the spill jet and buoyancy of the oil and gas in the jet can be clearly seen in images obtained by the ROV of the spill flow from the broken riser pipe as it laid on the seafloor (McNutt et al., 2011). At this time of the spill, before 3 June 2010, about 70% of the oil spill exited horizontally from the broken riser pipe. Within the image frame of a single ROV field of view, the oil and gas jet turned 90° upward and began to rise vertically. The transition length scale from momentum-dominated jet behavior, characterized by the horizontal flow, to buoyancy-dominated plume behavior, characterized by vertical ascent, is given by the jet-to-plume length scale L_M, given by $L_M = \frac{M_0^{3/4}}{B_0^{1/2}}$ where M_0 is the initial kinematic momentum flux, given by $M_0 = u_0 Q_0$ and B_0 is the initial kinematic buoyancy flux, given by $B_0 = (g(\rho - \rho_0)/\rho)Q_0$; u_0 is the initial velocity of the jet, Q_0 is the initial flow mixture flow rate of effluent, ρ_0 is the initial density of the effluent. For the DWH accident, L_M was on the order of 1 m, from which we can deduce that the initial buoyancy flux was greater than the initial momentum flux, and momentum was negligible. Moreover, the buoyancy flux of the DWH (Socolofsky et al., 2011) was some 10 to 100 times stronger than that associated with field of deep-sea thermal vents and chimneys (Lavelle, 1997). This also has important implications for determining the initial conditions of the spill plume and for gas bubble and oil droplet breakup, as the decay of turbulent dissipation rate is slower for a plume than a jet. Integral models capturing these equations were developed in early 2000s following (and based on) the DeepSpill experiment, which was conducted in 840 m water depth in the North Sea in the summer of 2000 (Johansen et al., 2003). Laboratory experiments included the work by Socolofsky and Adams (2002, 2003, 2005) on multiphase plumes and Masutani and Adams (2001) on bubble and droplet breakup in jets. Two integral models emerged, and both applied a Lagrangian approach to solving the integral equations (see, e.g., Lee and Chu, 2003). DeepBlow was developed by Johansen (2000, 2003) and included ambient stratification, gas dissolution, and separation of gas bubbles from the entrained plume of oil and seawater by the ambient currents. Clarkson Deep Oil and Gas (CDOG) grew out of models by Yapa and his research team (Yapa & Li, 1997; Yapa & Zheng, 1997; Zheng & Yapa, 1998). Both the DeepBlow (Johansen, 2003; Johansen et al., 2003) and CDOG (Chen & Yapa, 2003; Yapa & Xie, 2002; Zheng et al., 2003) models have been validated to the echo sounder data collected during the DeepSpill experiment. Several conclusions related to oil well accidents in deepwater stemmed from this exercise. First, the buoyant plume of oil, gas, and seawater formed an intrusion close to the seafloor. Though not directly observed, this was predicted by DeepBlow and CDOG, and intrusion formation is a reliable capability of these models, validated to a wide range of other laboratory data. The intrusion formed rapidly despite the weak ambient stratification because of the large entrainment rates that occur in strong crossflow resulting in a rapidly diluted plume. Hence, the majority of the oil droplet transport was by passive drifting with ambient currents and not fueled by a buoyant plume. Second, the oil first appeared on the surface much later than predicted by the computer models. This occurred because the modelers had used rise velocity predictions for clean bubbles rather than for dirty bubbles. Naturally occurring chemical

surfactant readily colonize bubble-water interfaces in the laboratory and the field. As bubbles contaminated with surfactants rise, the surfactants get pushed toward the lee of the bubble, setting up a gradient of surfactant concentration on the bubble-water interface. This nonuniform surfactant concentration results in Marangoni forces, which resist the free slip of the bubble-water interface with the ambient water, causing the bubble to have a no-slip boundary condition with the water. This increases the drag of the bubble, reducing its rise velocity, and shuts down internal circulations within the bubble, also reducing the mass transfer rates as internal convection ceases. When correlations for rise velocity for dirty bubbles were used (e.g., from Clift et al., 1978), the models agreed with the surfacing times observed in the field (Chen & Yapa, 2003; Johansen, 2003; Johansen et al., 2003). Third, because most of the vertical transport of the oil droplets to the surface was by passive advection in the ocean water column, the surface slick was distributed over a large area and was thin and diffuse (Johansen et al., 2003). Once the oil surfaced, it readily evaporated and was entrained by wind and wave action throughout the upper mixed layer; only 17% of the oil was found floating on the surface (Johansen et al., 2003). Because of the thin, diffuse sheen at the surface, each experiment dissipated quickly, and no in situ response was required to mitigate each experiment. The overall conclusion of the DeepSpill Joint Industry Project was that the oil spill models could adequately predict the dynamics and that much of the spill oil would remain suspended in the ocean water column or in thin, surface sheens.

5.1. Effects of Earth's Rotation

Recently laboratory studies have also considered the effect of Earth's rotation on the near-field plume of the DWH. The hint that planetary rotation could play an important role in DWH-type plume dynamics came as a surprise, given the scales that describe the setting. The importance of rotation relative to other dynamics is typically measured by the Rossby number given by $Ro = \frac{U}{fL}$ where U is a velocity scale, $f = 2\Omega\sin\theta$ measures the effective local background rotation (Ω is the rotation rate of the Earth and θ is latitude), and L is a length scale. Small Rossby numbers indicate rotational dominance. Buoyancy flux of the plume B, rotation f, stratification frequency N, and depth H are the essential parameters for a buoyant plume, and dimensional analysis leads to the buoyant velocity $(BN)^{1/4}$ and a second definition of the Rossby number using this velocity scale, $Ro = N/f$ (Frank et al., 2017). Based on the latitude of the DWH (27.8°N) and the local stratification ($N = 1.5 \times 10^{-3}\mathrm{s}^{-1}$ taken from Socolofsky et al. (2011)), the local Rossby number is ~20, a value that in traditional rotational fluid mechanics studies would suggest rotation can be ignored. The duration of DWH at 87 days, on the other hand, gives rotation ample time to present itself. There were also hints from previous laboratory studies, most notably Helfrich and Battisti (1991), about the importance of weak rotation in plume development, although the largest Rossby number they studied was 4.3.

Frank et al. (2017) conducted a number of lab plume studies in a ≈ 1.0 m diameter tank rotating around its axis at 0.1 to 1 rad.s^{-1}. They released saltwater downward and observed the precession. Their results confirmed the existence of the precession, albeit in unstratified conditions, and proposed a model for the steady precession based on mechanics similar to those of a spinning top. Their model predicted a precession rate that matched well with their experimental results. They also argued that plume precession was unavoidable regardless of how large the Rossby number, that is, no matter how weak the background rotation as long as it does not vanish. What required was that the plume release be sustained for intervals longer than the rotation period, which clearly emphasized the role played by the 87 day DWH duration. They also reasoned that the existing Rossby number measures were irrelevant to the problem, as they focused on the transit times of buoyant elements released at the wellhead, rather than on the duration of the event.

5.2. Detailed Observations of Multiphase Plumes

The increasing complexity of integral models and growing capability of computational fluid dynamics (CFD) models in the early 2000s drove laboratory observations beyond observation of bulk properties and toward an understanding of velocity and turbulence field in bubble plumes. Seol and Socolofsky (2008) developed a method to apply particle image velocimetry (PIV) to bubble plumes and reported the mean velocity field for bubble plumes in Seol et al. (2007). Seol et al. (2009) also observed the unsteady behavior of bubble plumes in stratification and showed that bubble plume wandering in large reservoirs results from interaction of the bubble column with large, turbulent coherent structures in the entrained ambient fluid. Bryant et al. (2009) used vortex-identification methods to characterize the turbulence in a bubble plume. They proposed that the modification to the turbulent energy cascade observed in their experiments and by others

(Bolotnov et al., 2008; Lance & Bataille, 1991; Rensen et al., 2005; Rensen & Roig, 2001; Simiano et al., 2006) results from turbulent energy production at the bubble scale. When this energy production falls within the inertial scale of the overall plume turbulence, the slope of the energy spectrum decreases from the classical −5/3 slope, though these experiments could not measure to the Kolmogorov scale of the bubble wakes. Hence, turbulence modeling of multiphase plumes will by necessity include some type of multiscale modeling to capture the turbulence production from the bubble-wake scale to the scale of the whole plume.

Methods to measure the full-field fluid motion of water in a multiphase bubble plume were just becoming mainstream when the DWH accident occurred (e.g., Simiano et al., 2006; Seol et al., 2007; Seol and Socolofsky, 2008; Bryant et al., 2009). These previous studies were effective at measuring the time-average velocity field but, unless very high spatial and temporal resolution were used, could not resolve the turbulence down to the Kolomogorov scale. Other past studies applied laser Doppler anemometry to a single point in a bubbly flow (e.g., Lance and Bataille, 1991) but were limited to low void fraction and required significant time to traverse a plume. Lai and Socolofsky et al. (2019) applied a new acoustic Doppler velocimeter that can take a short profile along its measurements volume (the Vectrino II by Nortek). Although previous applications of traditional acoustic Doppler velocimeter technology did not work well in bubbly flow, Lai and Socolofsky et al. (2019) showed that the Vectrino II could accurately measure the water-phase velocity in a bubble plume. Their measurements had 1 mm spatial resolution and were sampled at 50 Hz in a bubble plume with 1–4 mm diameter bubbles at void fractions from 0.7% to 1.8%.

Analysis of the turbulent velocity time series by Lai and Socolofsky et al. (2019) revealed several insights on the turbulent kinetic energy budget in a bubble plume. First, the probability density functions of the turbulent fluctuations and the characteristic frequency at which bubbles inject turbulent kinetic energy into the flow are similar to these properties measured in bubble columns, where there is no mean flow or shear entrainment. Second, the liquid turbulence is anisotropic, owing to the presence of the bubble wakes, with the turbulence intensity in the axial direction around twice the horizontal component values. Third, the turbulent kinetic energy production by air bubbles is much larger than that produced by mean shear at the edge of the bubble plume. And, fourth, more of the available work done by bubbles goes into the mean flow than into turbulent fluctuations on the plume centerline; whereas at the edges of the bubbly region, the mean velocity is low, and more of the work done by bubbles goes into turbulent fluctuations than the mean flow. They also observed three characteristic signatures in their time-series data: About 1% of the data represented direct passage of a bubble and the resulting high, negative fluid velocity filling its void after passage (this fraction also corresponds with the void fraction in the plume); about 10% of the data were in bubble wakes with velocities similar to the rise velocity of the bubbles, and the remaining approximately 90% of the data were in the turbulent liquid between bubble wakes and comprising the time-average Gaussian profile typically observed in buoyant plumes.

Observations of the bulk plume properties and their modulation by turbulence for an oil jet in crossflow was also conducted by Murphy et al. (2016). In these experiments, crude oil jets of droplets were created from a moving nozzle for oil with and without a pretreatment of chemical dispersant. Dissanayake, Gros, et al. (2018) determined that the contraction coefficient of the sinusoidally shaped nozzle was 0.4. Results without dispersant were similar to experiments in Socolofsky and Adams (2002), with largest oil droplets rising out of the plume and following trajectories given by the superposition of their terminal slip velocity and the ambient crossflow. Smaller oil droplets remained in the main plume, and when dispersant was injected, oil remained within the turbulent boundary of the plume far downstream.

Murphy et al. (2016) measured both the evolution of the droplet size distribution, using holography, and the dominant flow features of the plume, using PIV. Their results showed the importance of the classical counter-rotating vortex pair that typify a buoyant plume in crossflow (Jirka, 2004; Lee & Cheung, 1990; Lee & Chu, 2003). They also observed vertically oriented wake vortices on the bottom edge of the plume, typical of buoyant plumes in strong crossflow. They apply a trapping function from Friedman and Katz (2002) to determine the sizes of oil droplets that would be expected to be trapped within the counter-rotating vortex pair dominating the main flow of the plume. At a position around 1.50 m (400 orifice diameters) downstream of the orifice, 95% of the droplet sizes measured within the counter-rotating vortex pair are smaller than the critical diameter computed for trapping from their trapping function. This method

considers drag, lift, pressure gradients, inertia, added mass, and buoyancy and appears to accurately predict the trapping potential of these vortices.

Similarly, Chan et al. (2015) considered the trapping potential of the intrusion formation of a buoyant, multiphase plume in stratified crossflow. They used solid glass spheres as the dispersed phase and measured the spread of these spheres as they settled out of the intrusion layer. In these experiments, the particles initially spread out as the inner plume fluid detrains to form the downdraught plume. Depending on their rise velocity, the particles either continue into the intrusion layer with the continuous-phase fluid and settle out far downstream of the release, or they quickly rise out of the top of the plume and settle close to the release point. Chan et al. (2015) compared their results using the nondimensional slip velocity introduced by Socolofsky and Adams (2002). Applying their correlation to the DWH, one can predict that droplets of order 100 μm and smaller may be advected into the intrusion layer, whereas larger droplets would rise out of the detrainment region and advect to the sea surface close to the release point. Observations by Ryerson et al. (2011, 2012) support the conclusion that much of the oil release from DWH was in larger oil droplets, surfacing less than 2 km offset from the wellhead. Holographic camera images reported in Li and Vinhateiro (2015) also showed that small droplets of sizes 300 μm and smaller were transported into the intrusions. These observations corroborate these laboratory observations and their implications on the forces controlling droplet transport in plumes. However, because the droplet size distribution was not measured at the wellhead during DWH, more detailed conclusions require process-oriented simulation models.

5.3. Field Studies and the Effects of Gas Hydrates

Natural gas hydrates proved to be a major problem during the DWH accident, impacting the design and implementation of most all wellhead intervention measures. For example, the coffer dam failed due to its rapid filling and plugging with gas hydrate. At the same time, Anderson et al. (2012) showed that it was the formation of a physical surface where gas could collect that promoted hydrate growth for response activities. They showed that within the blowout plume itself, conditions were not favorable for hydrate formation due to the large dilution by entrainment of ambient seawater. Hence, it remained unknown whether hydrates played any role in controlling the fate of oil and gas released into the environment from the DWH.

The first laboratory study to consider this problem was conducted using a high-pressure water tunnel by the U.S. National Energy Technology Laboratory (Warzinski et al., 2014). They injected single bubbles into a counter-flowing, downward current and could suspend bubbles in a conical expansion. They imaged the bubbles using a single, high-speed camera. From the camera video, they could track the bubble shrinkage rate over time and image the formation of hydrate shells on the bubbles. When the hydrate shell formed, the wave oscillations on the bubble-water interface ceased, and the bubbles appeared to be frozen in shape (rigid). This occurred even after a very thin film of hydrate formed. Warzinski et al. (2014) reports on the detailed observations of a methane bubble that undergoes hydrate formation. Because of the fact that hydrate does not form readily in the laboratory until the background dissolved gas concentration in the tank reaches the solubility of the methane hydrate and because of uncertainty in tracking the shrinkage rate of bubbles with a single camera, detailed dissolution rates could not be reported. However, this study did show the interesting hydrate plate dynamics of hydrate-armored bubbles and pioneered a new measurement method for identifying hydrate on bubbles in the ocean.

Wang and Socolofsky et al. (2015) capitalized on this method to design a new imaging system to study hydrates on bubbles released from subsea natural gas seeps. They mounted two high-speed cameras in a stereoscopic arrangement so that they could have reliable image scale measurements over a large depth of field. They validated the system in the laboratory (Wang & Socolofsky, 2015) and deployed the system from the ROV Hercules on the E/V Nautilus in Wang et al. (2016). The Wang et al. (2016) paper reports on their research cruise to Mississippi Canyon lease block 118 and Green Canyon lease block 600, both primarily thermogenic gas seep systems at about 950 m depth on the continental flow of the Gulf of Mexico.

Wang et al. (2016) uncovered several important insights related to bubble dynamics at natural seeps. At all seep sites, hydrates formed quickly on the bubble-water interface (within <2 m of rise above the seafloor), and bubbles appeared similar in shape to those simulated by Warzinski et al. (2014). The water depth corresponding to the onset of gas hydrate stability was about 370 m depth or 590 m above the sea floor; the hydrate subcooling at the release was about 12.5°C. Gas bubble sizes were also similar at each seep site, with the

median bubble diameter ranging from 3 to 5 mm. Measured bubble rise velocities were significantly slower than those predicted by empirical equations (Clift et al., 1978). This could not be attributed to the higher density of the thin hydrate shell. Instead, because they collected stereoscopic data, the three-dimensional trajectory of each bubble in the water column could be tracked. Fast-rising bubbles, those that matched correlations in Clift et al. (1978) followed helical paths, while bubbles 40% slower than predictions from Clift et al. (1978) followed zig-zag paths, locked to a single, vertical plane. This dependence of the rise velocity on the bubble path had been observed previously in the laboratory by Wu and Gharib (2002) and Tomiyama et al. (2002), and this behavior appears to be a completely random (unpredictable statistics) result of the instability of the bubble at formation at the release.

The bubble size measurements were made at the sea floor and following the bubble column up to 250 m above the seafloor (Wang et al., 2016). Shortly above the seafloor, the bubble column spread out enough that only part of the full plume could be imaged at each height. Measurements focused on the larger bubbles that follow similar paths along the upstream edge of the bubble column. Comparing the bubble size distributions at each height, they could evaluate a shrinkage rate and, after accounting for gas expansion by pressure relief, the shrinkage rates compared to predictions from empirical formulas for mass transfer in Clift et al. (1978). Bubble shrinkage rates at the seeps surveyed in Wang et al. (2016) agreed well with dirty bubble mass transfer rates and were significantly slower than the rates for clean bubbles. Zhao, Boufadel, et al. (2016) used the VDROP-J model to track the bubble size distribution of bubbles from a bubbly jet and found that dissolution in the surrounding converts a bimodal distribution into a monomodal distribution. Essentially small bubbles disappear rapidly, and the large bubbles decrease in size to occupy an intermediate model of the initial bubble size distribution.

Wang et al. (2016) also analyzed the spreading rate of the bubble column with height above the seafloor. Buoyant jets and plumes spread out linearly with height, with a spreading rate of order 0.1 m spread per m of rise. Bubble columns emanating from these natural seeps spread out at a much slower growth rate, indicating that their spreading is not dominated by a shear entrainment process. Wang et al. (2019) further analyzed this problem in the laboratory, studying the dynamics of bubble plumes with similar source flow rate and bubble size to the natural seeps observed in Wang et al. (2016). Wang et al. (2019) showed that the spreading rate of the bubble column followed a power law expansion rate proportional to $z^{1/2}$, which is indicative of diffusive spreading. They further showed that bubble columns from weak plumes, like natural seeps, grow by an apparent turbulent diffusivity related to the lateral excursion of the wobbling bubbles and that their dynamics cannot be predicted by a classical integral model based on entrainment.

Several conclusions for oil well blowout plumes can be derived from these studies. If hydrate formation is present, it will likely result in a thin, plated shell on the bubble water interface. This shell gives the bubble a frozen (rigid) physical structure, similar in character to dirty bubbles with a no-slip boundary condition. Their rise velocities and mass transfer rates, therefore, should be expected to either agree with those of dirty bubbles or perhaps yield lower values due to the potential that the hydrate film limits mass transfer of the free gas inside the bubble to the ocean water column (and thus the droplet does not decrease much in size). Rise velocities may also be lower if bubbles follow a zig-zag, rather than helical, rise path. Natural seeps, having small gas fluxes, show almost not entrainment and their dynamics are described by the Lagrangian rise of individual bubbles. This is similar to the predicted behavior of gas bubbles and oil droplets rising out of the intrusion layer of an oil well blowout plume. These weak plumes do not exhibit entrainment and instead spread out by the apparent turbulent diffusion of the wobbling trajectories of the bubbles and the diffusivity of the ambient turbulence. This lends added support to the hypothesis that particle transport above the initial intrusion of a multiphase plume in stratified crossflow may be modeled as passive Lagrangian transport.

5.4. Computational Fluid Dynamics Models

In recent years, the continual growth of computing power has made the CFD approach a feasible tool for studying the detailed fluid dynamics in various complex environmental and engineering flows. A CFD approach usually involves numerically solving the three-dimensional Navier-Stokes equations of a certain form (which varies with the choice of the specific CFD technique). Based on the range of scales directly computed, the CFD models may be categorized into three major types, that is, the RANS model, the LES model, and the direct numerical simulation (DNS) model (Lesieur & Metais, 1996; Meneveau & Katz, 2000; Moin &

Mahesh, 1998; Pope, 2000). RANS models compute only the evolution of the mean plume, with the turbulent transport unresolved but parameterized by different closures, mostly the k-ε model. For engineering applications, many CFD tools are built upon the RANS model considering its low computational cost required for only capturing the mean flow, but the detailed turbulence structures cannot be obtained. Conversely, DNS models attempt to directly resolve the turbulence motions at all the relevant scales (ideally down to the Kolmogorov scale), therefore, do not require a closure for the turbulent transport. However, the high computational cost required by DNS makes it suitable to simulate only the low Reynolds number plumes, useful for canonical studies but infeasible for practical applications. Falling between RANS and DNS, LES models are able to directly resolve a range of large- and intermediate-scale turbulent motions (with a cut-off scale depending on the numerical grid resolution) and only requires modeling the unresolved subgrid-scale effect. LES combines the advantages from the RANS and DNS concepts and has evolved into a promising tool for simulating various engineering and environmental flow problems. As the subgrid scale of the LES decreases, LES results approach those of DNS.

As the experimental work would suggest, the fundamental issues for numerical simulation of dispersed flows are turbulence closure and bubble/droplet modeling. Regarding the former, at the time the DWH spill occurred, there was already a consensus on the limitations of RANS simulation together with isotropic turbulence closure to predict dispersed flows. Despite some relevant RANS-based studies (e.g., Laın et al., 2002; Sokolichin et al., 1997), LES became the prevalent modeling approach for practical multiphase flow scenarios with the arrival of the new century. A good review of research conducted before DWH on LES for dispersed flows can be found in Dhotre et al. (2013). DNS before DWH was heavily constrained on the bubble/droplet count (e.g., Bunner and Tryggvason, 2002, 216 bubbles; Roghair et al., 2011, 16 bubbles). Methods such as volume of fluid or level set can solve the dynamic interface between the bubble/droplet and the continuous phase, including break up and coalescence. The inherent complexity and high resolution needed for these purposes ties the interface-solving approach to DNS.

Before DWH, LES of dispersed flows showed a steady development, albeit with some general flaws: (a) validation merely focused on mean velocities, (b) available data set reduced to the study of single plumes in stagnant, nonstratified tanks, and (c) unclear bounds for the modelling assumptions. A popular approach for the treatment of the dispersed phase in LES is the Eulerian-Eulerian (EE) method (e.g., Milelli et al., 2001; Ničeno et al., 2009), in which both phases share a common Eulerian framework. The main assumption is that the mix of bubbles/droplets with the continuous matrix creates a homogeneous mixture, characterized by a volume fraction and a density. EE has been successful in predicting the average flow properties and the large-scale turbulence, its drawbacks being high numerical diffusion and the omission of key phenomena such as entrainment. Prior to the DWH spill, there were a small number of works based on the Eulerian-Lagrangian (EL) approach (e.g., Hu and Celik, 2008; Mazzitelli and Lohse, 2009; Sungkorn et al., 2011). EL respects the discrete nature of the dispersed phase, which is displayed in a Lagrangian framework, independent of the computational mesh for the continuous phase. The bubbles/droplets are modeled using point particles. The interaction between the Eulerian and Lagrangian phase occurs via the implementation of interfacial forces. Two main issues challenged the application of EL methods: The computational cost implied in the mapping of the Lagrangian particles and the complex coupling between the two phases. In the wake of the DWH accident, both EL and EE models experienced significant advancement, improvement, and application to understand the complex flow of the DWH near-field plume.

5.4.1. Turbulence-Resolving Models

Following the DWH accident, the LES numerical modeling technique has been successfully applied by several research teams to study the detailed flow physics in multiphase buoyant plumes, both at laboratory and field scale (Chen et al., 2018; Fabregat et al., 2015; Fabregat Tomàs et al., 2016a; Fraga & Stoesser, 2016; Fraga, Stoesser, Lai, et al., 2016; Yang et al., 2016). These LES studies model the seawater flows as a continuous phase carrier flow using the Eulerian approach by solving the filtered Navier-Stokes equations and treat the buoyant particles (i.e., gas bubbles and oil droplets) as the dispersed phase being transported by the carrier flow. The concentrated particles in turn provide buoyancy force to drive the plume rise upward. These models differ in the way that the transport of dispersed particles is modeled and can be categorized into two types. Fraga and Stoesser (2016) and Fraga, Stoesser, Lai, et al. (2016) modeled the dispersed particles as point particles and solved their motions using a Lagrangian approach by solving the Newton's second law for each individual particle. This EL modeling strategy allows to track the detailed motions of each

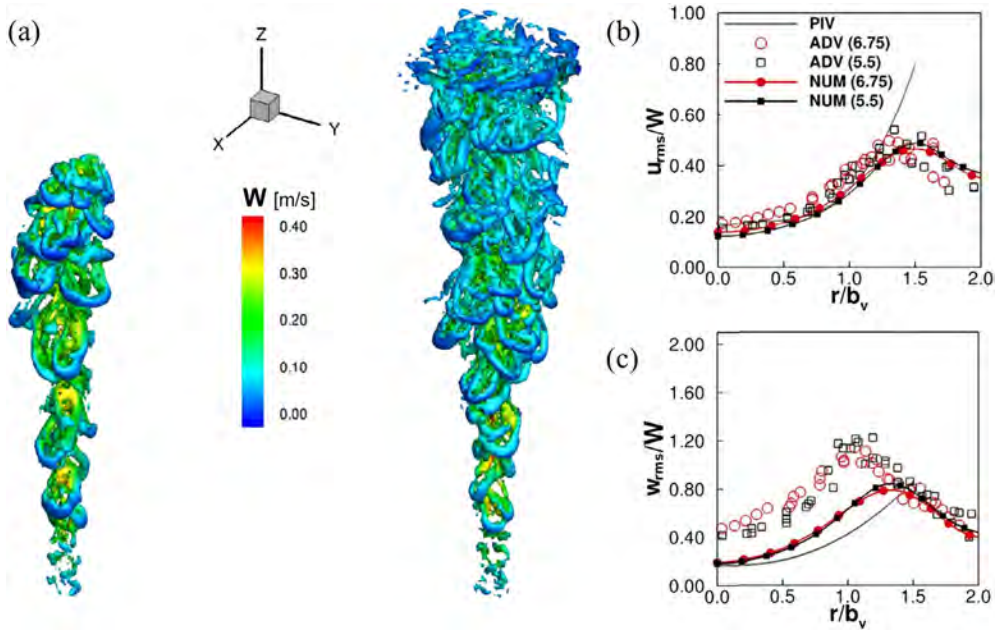

Figure 8. Sample simulations results by Fraga, Stoesser, Lai, et al. (2016) for (a) vortical structures visualized by the Q criterion in the simulated bubble plume and colored by vertical velocity (left $t = 5$ s, right $t > 20$ s), (b) comparison of simulated and measured normalized root-mean-square velocities in the radial direction, and (c) comparison of simulated and measured normalized root-mean-square velocities in the vertical direction. The model captures well the radial turbulence fluctuations but underpredicts the vertical fluctuations due to a lack of bubble-generated turbulence in the numerical simulations. Overall, the model captures well the time-averaged and radial turbulence properties of the plume.

individual particle and includes the effects of various hydrodynamic forces acting on the particles, for example, buoyancy, fluid stress, added mass, drag and lift. However, the high computational cost also limits its application to small-scale numerical experiments. Nevertheless, many useful physical insights are obtained from such model to help improve our understanding on the detailed particle dispersions as well as integral behavior of the plume (Fraga & Stoesser, 2016; Fraga, Stoesser, Lai, et al., 2016).

Instead of tracking the motions of individual particles, Fabregat et al. (2015), Fraga and Stoesser (2016), and Yang et al. (2016) used a EE strategy for modeling the plume dynamics, in which the transport of dispersed particles is modeled by solving the Eulerian transport equation of the particle concentration function. These EE models have been shown to well capture the macroscopic dynamics of the plume for various scales, such as the peeling and trapping processes when the buoyant plumes interact with the stably stratified ambient fluid environment, the vertical development of the plume size, and the radial profiles of the vertical velocity.

5.4.2. Eulerian-Lagrangian LES Models

Fraga, Stoesser, Lai, et al. (2016) developed an Eulerian Lagrangian algorithm (BubLPT) for LES of dispersed flows and validated it for bubble plumes to the data. The main contribution of this research with regard to its predecessors was (a) use of a dynamic stencil for the liquid-gas coupling, (b) use of delta functions (Yang et al., 2009) for the Eulerian-Lagrangian transfer of properties, and (c) grid-independent scaling of the forces. This new algorithm was used to predict the dynamics of a bubble plume previously studied experimentally (Lai & Socolofsky, 2019). The results showed a good prediction in terms of first-order flow statistics, integral properties of the plume, entrainment mechanisms, and slip velocity.

The limitations of EL-LES were also explored by Fraga, Stoesser, Lai, et al. (2016). The mesh convergence showed that beyond a certain bubble-to-mesh size ratio, further refinement does not improve the results. More importantly, Fraga, Stoesser, Lai, et al. (2016) provided validation of the second-order statistics. The horizontal turbulent fluctuations showed a remarkable agreement, whereas an important underprediction was found in the streamwise axis. This difference was attributed to the scale-separation inherent to bubble plumes. BubLPT is able to predict the instantaneous turbulent structures generated at the plume's shear

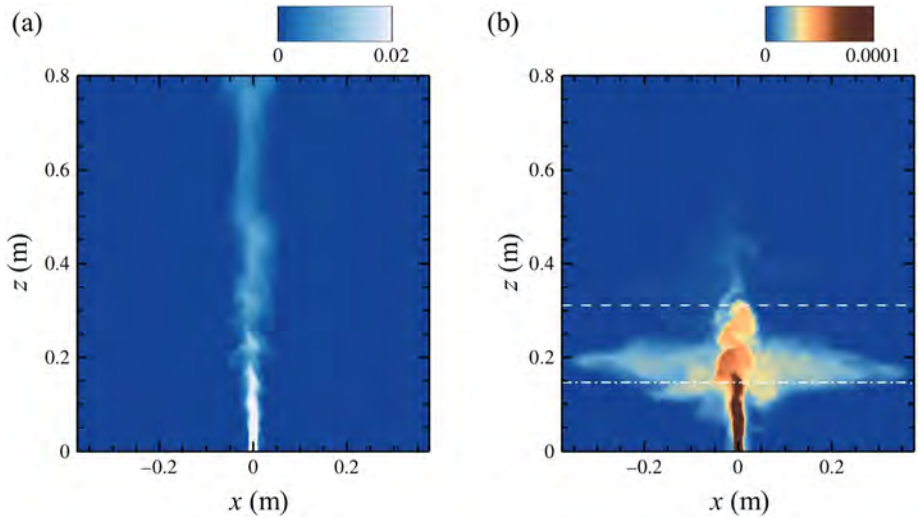

Figure 9. Simulation results for a bubble plume in linearly stratified water from Yang et al. (2016) for laboratory cases similar to Socolofsky and Adams (2005): (a) bubble concentration and (b) passive tracer concentration; horizontal lines indicated peel and trap heights from laboratory experiment, which are in good agreement with the numerical simulations.

layer. However, since the boundary layers of the individual bubbles are not solved, the bubble-scale wakes cannot be accurately described by EL-LES (see Figure 8).

BubLPT was used to study the sensitivity of the bubble plumes to changes in bubble size, diffuser size, gas flow rate (Fraga & Stoesser, 2016), or presence of a crossflow (Mitrou et al., 2018). It was found that bubbles self-arrange in space within the plume according to their sizes, and the structure of the secondary flow induced by a bubble plume in crossflow was described. Fraga and Stoesser (2016) linked the 3-D LES data set with integral plume properties to inform coefficients adopted by integral 1-D models. The influence of the bubble size on the entrainment coefficient is particularly relevant.

From a computational perspective, EL algorithms bear the extra challenge of a spatially unbalanced load of Lagrangian particles, which significantly deteriorates the scalability of regular MPI parallelization. Ouro et al. (2019) developed hybrid strategies specifically for EL algorithms, achieving speedups on the order of 30–70% when compared to pure message passing interface (MPI) parallelization. However, EL LES remains constrained to a tractable number of bubbles or droplets and to date has been applied only to study laboratory-scale scenarios.

5.4.3. Eulerian-Eulerian LES Models

LES models based on the EE approach have been applied to laboratory-scale experiments, idealized field-scale experiments, and regions of the full-scale DWH blowout. At the laboratory scale, Figure 9 shows some sample results obtained from the Eulerian-Eulerian LES model of Yang et al. (2016), scaled to the laboratory experiments in Socolofsky and Adams (2003, 2005). Yang et al. (2016) also combined statistical analysis to evaluate the turbulent plume entrainment coefficients for application in integral plume models, and they proposed a new plume peeling process model that is derived based on control volume analysis and assessed using LES data. The computational efficiency of the Eulerian-Eulerian model makes it feasible for simulating real-scale plumes close to the condition of DWH blowout. For example, Chen et al. (2018) combined the two Eulerian-Eulerian LES models for the nearfield plume dynamics from the source of the blowout at 1,500 m depth and the far field oil plume dispersion in the uppermost 50 m layer of the ocean over extended horizontal domain of O(10) km (Chen et al., 2016) and studied the effects of dispersant applications on the vertical and horizontal transport of oil droplets.

Recently, the Eulerian-Eulerian LES modeling framework is further advanced with additional important features being incorporated. For example, Aiyer et al. (2019) adopted the method of particle population balance model (Coulaloglou & Tavlarides, 1977; Prince & Blanch, 1990; Tsouris & Tavlarides, 1994; Wang &

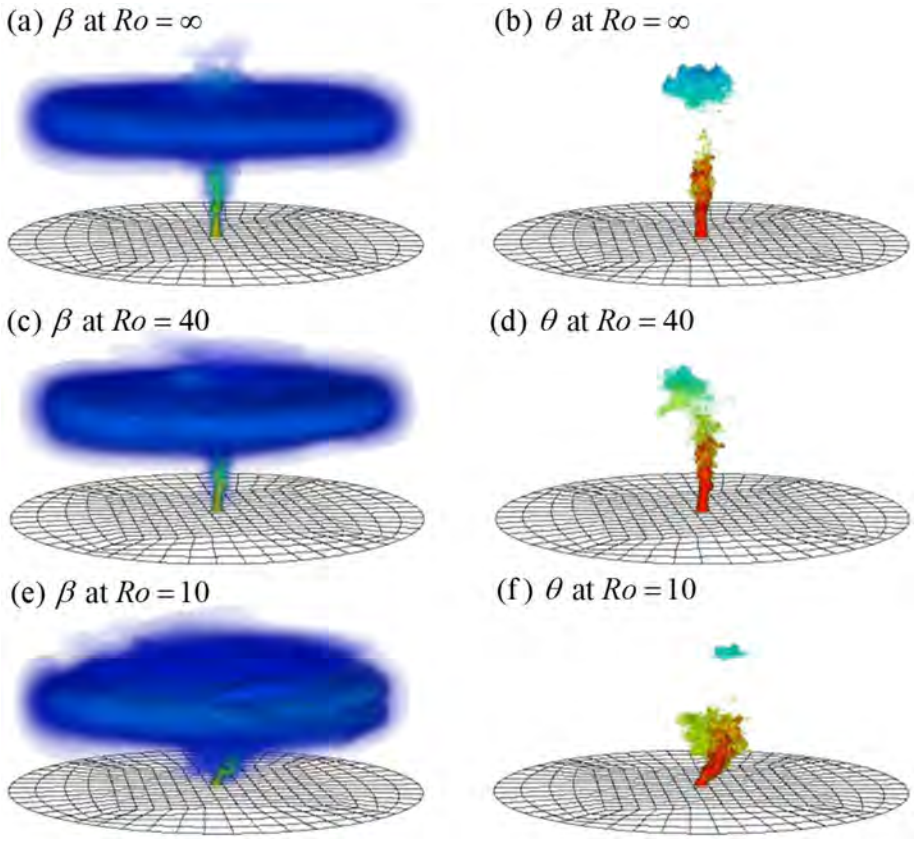

Figure 10. Plume structure in rotational settings. The left column shows a passive tracer distribution, and the right column shows buoyancy anomaly, both emanating from a point source in the bottom middle of the domain. The top row is a nonrotating experiment, the middle row has weak rotation ($Ro = 40$) and the bottom row stronger, if still weak, rotation ($Ro = 10$). The DWH setting was characterized by $Ro = 20$. Note the suppression and broadening of the peel height and intrusion layer with increasing rotation. Taken from Fabregat Tomàs et al. (2016b).

Wang, 2007; Zhao, Boufadel, et al., 2014; Zhao, Torlapati, et al., 2014) and developed a Eulerian-Eulerian LES model for simulating polydisperse droplet evolution.

The dispersed phase equations have themselves been studied for their properties. Deremble (2016) used classical method-of-continuation techniques to examine the dependence of azimuthally averaged dispersed phase structure on background rotation strength. He found with the inclusion of rotation that plume structure bifurcated from the expected, nonrotating structure to an off-axis structure that, surprisingly, exhibited mean down-drafts directly over the wellhead. Similar structures were found by Fabregat Tomàs, Poje, et al. (2017). Deremble's solutions also suggested the presence of multiple equilibria, that is, the possibility that mean plume structure could exist in more than one configuration for identical parameter settings.

Fabregat et al. (2015), Fabregat Tomàs et al., (2016a, 2016b), and Fabregat, Deremble, et al. (2017) examined numerical solutions of the dispersed phase equations both with and without rotation and in single and multiphase settings. Their results demonstrated for DWH-like settings that rotation induced a number of changes in point source plume structure, from suppression of the so-called “peel height” to broadening of the plume width. Perhaps the most profound effect of rotation, however, was the presence of a plume anticyclonic precession, that is, an off-axis tilt to the plume that moved in a clockwise fashion about the wellhead (see Figure 10). It was this feature that led to the broadening of the plume width. The numerical solutions allowed for a rather complete diagnosis of the plume dynamics and illuminated the role of background rotation. Specifically, fluid was drawn to the wellhead by the low pressures generated by the buoyant plume materials near the wellhead. These fluid parcels were imbued with a weak, but nonetheless nonzero, rotation whose source was the planetary background. As water parcels converged on the wellhead, angular

momentum conservation resulted in an amplification of their spin into a strong cyclonic flow. This tended to block the radial influx of new fluid, even while the buoyant fluid over the wellhead was still impelled to ascend. The plume achieved its needed vertical flux by breaking symmetry and developing the precessing plume structure. Interestingly, Fabregat Tomàs, Poje, et al. (2017) observed persistent downdrafts over the wellhead, reminiscent of the structure computed by Deremble (2016), whose radially symmetric off-axis solutions could be interpreted as the time averaged structure left behind by a precessing plume.

6. Chemical and Thermodynamic Models of Petroleum Mixtures

Dissolution is critically important both to the gas phase and live-oil liquid phase petroleum compounds emanating from the spill source (Kessler et al., 2011; Ryerson et al., 2011, 2012). Integral models already considered the nonideal behavior of gas at high pressure (Johansen, 2003; Zheng et al., 2003) and dissolution (Zheng & Yapa, 2002) because these processes are necessary to accurately predict the buoyancy flux in the oil and gas plume and the subsequent Lagrangian transport above the intrusion layer as pressure decreases as the bubble rise in the ocean. However, because dissolution only weakly affects buoyancy for the liquid petroleum phase, dissolution from the complex mixture of petroleum chemicals in a live crude oil were ignored, and the oil droplets were treated as inert particles. While this may still be acceptable to understand the fluid dynamics of a blowout plume, dissolution from the MC252 plume partitioned a large number of petroleum chemicals throughout the water column (Spier et al., 2013), and dissolution from the initially liquid-phase petroleum was critical to predict this.

A live petroleum fluid at depth in the ocean does not behave as an ideal fluid. Petroleum engineers have dealt with this problem for decades, and the approach in McCain (1990) has been the foundation of much of the innovations for oil well blowout modeling since DWH. Petroleum engineers deal mostly with oil and gas in pipelines, where intrusion of seawater is minimized and where accurate prediction of density and gas/liquid phase equilibrium is most important. McCain (1990) utilizes the Peng-Robinson cubic equation of state (Peng & Robinson, 1976; Robinson & Peng, 1978) and tabulates the necessary thermodynamic properties of several hydrocarbon molecules for use with this equation of state. The Peng-Robinson equation of state handles chemical mixtures and can predict the mixture density and the fugacities of each chemical component in the mixture at a given temperature and pressure.

The Peng-Robinson equation of state with several additional physical and thermodynamics models to address oil droplets has been implemented since DWH in the Texas A&M Oil spill Calculator (TAMOC). TAMOC is a comprehensive suite of models to predict gas and oil droplet dynamics and to implement them in both a nearfield Lagrangian particle tracking model and nearfield integral model. The integral models are based on the approaches developed earlier by Crounse et al. (2007) and Socolofsky et al. (2008) for double-plume integral models and by Johansen et al. (2003) and Zheng et al. (2003) for blowout plumes in crossflows. The complete modeling system is described in Dissanayake, Gros, et al. (2018), including all of the plume model validation. The chemical and thermodynamic models are documented in Gros et al. (2016), including validation to samples taken at the wellhead of the DWH oil.

To predict the dissolution of rising oil droplet, two additional parameters beside the density and fugacity are required: the solubility and mass transfer coefficient for each chemical component of the mixture at the droplet-water interface. Before DWH, McGinnis et al. (2006) summarized an approach to adjust solubilities from standard conditions to conditions at high pressure, different temperature, and considering the effects of salinity. They studied methane dissolution from natural seep bubbles. Henry's law relates the water solubility of a gas in a gas mixture under ideal conditions to the partial pressure of that gas in the mixture. At high pressure, the partial pressure is replaced by the real-fluid fugacity of each compound in the mixture (King, 1969); the Henry's law constants are adjusted from standard conditions to the in situ temperature (King, 1969), and the correction for salinity is by a Setschenow coefficient (Krichevsky & Kasarnovsky, 1935). This model gives the solubility $C_{s,i}$ of each chemical compound in a mixture as follows:

$$C_{s,\,i}=H_0F_i\exp\left[\frac{1}{R}\frac{\partial H_{sol,\,i}}{\partial T}\left(\frac{1}{T}-\frac{1}{T_0}\right)\right]\exp\left[\frac{\overline{\mathrm{v}}_i(P_0-P)}{\mathrm{RT}}\right]10^{-(SK_{s,\,i})/M_{\mathrm{sw}}} \tag{5}$$

where H_0 is the Henry's coefficient at standard conditions, F_i is the fugacity of the ith component of the

mixture, T_0 and P_0 are the temperature and pressure at standard conditions, R is the universal ideal gas constant, T and P are the in situ temperature and pressure, S is the in situ salinity, $H_{sol,i}$ is the enthalpy of solution for the ith component of the mixture, $\bar{v}_i$ is the molar volume at infinite dilution of chemical component i, $K_{s,i}$ is the Setschenow coefficient for the ith component of the mixture, and M_{sw} is the molecular weight of the seawater. The TAMOC model computes F_i using the Peng-Robinson equation of state (Peng & Robinson, 1976) with volume translation (Lin & Duan, 2005) to improve the prediction of density from the Peng-Robinson cubic equation of state.

The Peng-Robinson equation of state is a framework to compute thermodynamic properties of real mixtures; yet, it requires many chemical properties as input. Several modules in TAMOC compute these essential parameters. The temperature-dependent binary interaction coefficients are estimated by a method in Privat and Jaubert (2012) and by Pedersen et al. (2014). Thermodynamic properties for each component considered in the mixture are taken from the literature, where available, or estimated from various group-contribution methods. Much of the literature data in TAMOC is from McCain (1990) and Poling et al. (2001). TAMOC uses methods by Avaullee et al. (1997) and Gharagheizi et al. (2011) to estimate missing acentric factors and critical-point properties and a method in Hine and Mookerjee (1975) for missing Henry's coefficients. To model petroleum fluids, which contain thousands to tens of thousands of individual chemical compounds, TAMOC utilizes individual chemical compound data for many known petroleum components and lumps other groups of compounds into pseudo-components that behave in a similar way. For more details, see Gros et al. (2016) and the supporting information, therein. In the end, these chemical equations predict the density of a petroleum fluid mixture (liquid or gas phase), the solubility in seawater of each chemical compound in the mixture and can compute the phase equilibrium of the mixture between gas and liquid phases following the approach in Michelsen and Mollerup (2004).

The rate of mass exchange by dissolution between a bubble or droplet and the ocean is modeled using a mass transfer formulation. Rather than solving for the spatially and temporally variable dissolution across the whole interface of a bubble or droplet, the mass transfer coefficient integrates this exchange into an average that can be expressed by the simple equation given by

$$\frac{dm_i}{dt} = -A_s \beta_i \left(C_{s,i} - C_{a,i} \right) \tag{6}$$

where m_i is the mass of component i in a bubble or droplet, A_s is the surface area of the bubble or droplet, $C_{s,i}$ is the solubility of component i in the surrounding seawater, $C_{a,i}$ is the concentration of component i in the seawater far from the interface of the bubble or droplet, and β_i is the mass transfer coefficient of component i. The term β_i includes the physical processes of molecular diffusion within the chemical boundary layer at the particle interface, spatial and temporal variability integrated over the particle interface, and the convection in the turbulent wake behind the bubble or droplet. Hence, β_i depends on the bubble or droplet size, shape, rise velocity, and the molecular diffusivity of the ith compound. Molecular diffusivities in TAMOC are taken from literature values and by a method in Hayduk and Laudie (1974); empirical equations for β_i are from Clift et al. (1978) for dirty bubbles and Johnson et al. (1969) for clean bubbles.

The remaining properties needed to simulate a real blowout scenario are the viscosity and interfacial tension of the petroleum gas or liquid phase with water, as needed by the model to compute size distributions in the initial jet breakup region. Viscosity is estimated by a correlation in Pedersen et al. (2014) and interfacial tension from Danesh (1998). All of these thermodynamic equations were validated to the DWH oil in Gros et al. (2016) using 131 individual molecules and an additional 148 pseudo components, derived from two-dimensional gas chromatography (GC × GC) of samples collected at the DWH wellhead (Reddy et al., 2012). A simpler model involving 11 pseudo-components and tuned to the DWH oil can be found in Zick (2013). Data for the Gros et al. (2016) model are publicly available through the Gulf of Mexico Research Initiative Information and Data Cooperative (doi: 10.7266/N7PZ56RH). During the early days of a spill, however, this kind of detailed information is not likely available. Instead, one may need to build an oil model from a distillation curve and saturates, aromatics, residues, and asphaltenes analysis. Gros et al. (2018) adapted the correlations and group contribution methods summarized above to estimate pseudo component properties for the TAMOC

Peng-Robinson equation of state from such distillation cut data, as found, for example, in the NOAA Oil Library (https://github.com/NOAA-ORR-ERD/OilLibrary).

The validation in Gros et al. (2016) underscored the importance of light hydrocarbons (e.g., compounds commonly in the gas phase at standard conditions, such as methane, ethane, and propane) dissolved in the liquid phase at the spill source at 1,500 m in the Gulf of Mexico. This liquid, live-oil (crude oil with significant gas and volatile compounds dissolved in it) represents the initial conditions at the spill source for any model. How this live-oil flow rate, which might be measured in situ by visual or other methods, relates to a dead oil (crude oil after equilibrium with the atmosphere at standard conditions) mass flux is critically sensitive to the mixture composition assumed in the model and is important as fine paid by the responsible party are based on volume of dead oil spilled. The advances summarized here help to address this question and were critical for predicting the fate of light petroleum compounds in the ocean water column and atmosphere.

7. Empirical and Integral Models

Some of the scale equations (e.g., empirical equations for trap and peel height) were used early on following the DWH spill to explain the observed subsurface intrusion layer (Socolofsky et al., 2011) and to initialize far-field particle tracking models (North et al., 2011, 2015) before the improved integral models were ready to make accurate hindcasts. The main research innovations following DWH for integral models were made through development and validation of TAMOC (Gros et al., 2017, Dissanayake, Gros, et al., 2018). Premathilake et al. (2016) also improved simulation of the zone of flow establishment for a gas release, and industry models were also improved to hindcast the dynamics of the DWH (Socolofsky et al., 2015; Spaulding et al., 2017).

Shortly after the DWH, Socolofsky et al. (2011) applied empirical equations from Socolofsky and Adams (2002, 2003, 2005) to the DWH. They showed that for deep ocean currents less than 0.1 m/s, the DWH plume would be stratification dominated, with the intrusion height dependent on the buoyancy flux, slip velocity of gas bubbles, and the ambient buoyancy frequency. They used measured CTD profiles to estimate the buoyancy frequency and computed trap heights in agreement with fluorescence profiles obtained in the intrusion layer within the far field region of the spill (e.g., as reported in Spier et al., 2013). At the time, there were no reliable models to predict oil droplet size, and they relied on the fact that the gas bubbles, with their much larger slip velocity, should be the dominant multiphase component of the plume and the main factor determining u_s in the empirical equations. This work validated the idea that the primary subsurface intrusion at 1,100 m depth in the Gulf of Mexico was formed by the arrest of a buoyant plume of gas, oil, and entrained seawater in the stratified ocean but to make predictions of mass partitioning among dissolved, gas, and liquid phases and between the intrusions and the sea surface, process-oriented integral models were needed.

The most important improvements to integral models were the chemical and thermodynamic equations to handle complex petroleum mixtures (see section 5.4), which allowed models to predict dissolution from both the gas and liquid phase bubbles and droplets in the transit from the seafloor to the surface. Development of the TAMOC model also included two incremental improvements to integral model physics. First, TAMOC improved entrainment models in crossflow by combining the Eulerian-based shear entrainment model in Jirka (2004) with the forced-entrainment algorithm in Lagrangian models by Lee and Cheung (1990). Dissanayake, Gros, et al. (2018) showed that when an adaptive step solver for stiff differential equations is used, these two models better match the initial mixing plumes in crossflow than the original algorithms in the Lagrangian integral model approach (e.g., Lee and Chu, 2003). Second, Dissanayake, Gros, et al. (2018) present the only detailed explanation in the literature of how to account for loss of bubbles at the upstream side of a multiphase plume in crossflow. They also showed that as bubbles and droplets are transported away from the plume centerline, their contribution to the buoyancy flux of the plume must be reduced. They calibrate their approach to the experiments in Socolofsky and Adams (2003) and validate the model to oil jets in crossflow reported in Murphy et al. (2016).

To validate predictions of integral models at field scale, TAMOC was applied to predict a short period of the DWH accident during which detailed observations were also made (Gros et al., 2017). All of the model coefficients were calibrated and validated to the historical and new laboratory and field data available before

DWH. The chemical and thermodynamic model in TAMOC was used to predict the conditions of the source fluid using the oil composition from Gros et al. (2016). The dead oil flow rate was taken from the Oil Budget Calculator (Lehr et al., 2010), with the reported amount of oil collected by response at the source removed (Aliseda et al., 2010). Gros et al. (2017) simulated the conditions on 8 June 2010 , during the period in which subsea dispersant injection was active. They used the reported daily dispersant injection amount to estimate an average dispersant-to-oil ratio by assuming uniform mixing at the source and a constant injection rate. The interfacial tension of the oil and gas in water was reduced by a factor of 5.4, based on the estimated DOR and experimental results in Abdelrahim and Rao (2014). This flow rate and the oil properties predicted by TAMOC were provided to VDROP-J to estimate the initial gas bubble and oil droplet size distribution. Because the oil and gas rapidly cool to ambient conditions after entrainment of ambient seawater in the zone of flow establishment, these initial conditions were estimated at the in-situ temperature. One CTD profile from station B54 from the R/V Brooks McCall on 30 May 2010 was used throughout the simulations; currents were obtained from an acoustic Doppler current profiler operating less than 1 km from the crippled wellhead (see the supporting information in Gros et al. (2017) for all details of the simulations).

These initial conditions were used to drive TAMOC simulations for a Lagrangian plume integral model to the intrusion layer, followed by Lagrangian particle tracking of gas bubbles and oil droplets until the particles dissolved, they reached the sea surface, or they flowed out of a near-field cylinder 10 km in radius. During the simulations, each bubble and droplet was allowed to undergo phase transitions as dissolution changed the composition, and particles with a mixed gas and liquid phase were assumed to stay together as a single multiphase particle. The concentration and mass flux of dissolved petroleum compounds in the intrusion layer was tracked to the end of the near field. Mass fluxes to the atmosphere under steady state conditions were estimated by standard empirical relations for oil slick volatilization at the sea surface under the conditions representative of 8 June 2010.

Model results of this kind should not be compared directly to concentration measurements for grab samples in the environment. This is a well-known aspect of geochemical measurement in the ocean and is due to the unknown amount of mixing between the release and a single sample in the unsteady, stirred, and turbulent ocean. Moreover, the model predicts average, integral quantities. Instead, one may compare the composition of a sample to the composition of the source fluid to determine the fraction of each compound that has reached the sample location. This approach is facilitated by computing fractionation indices. For example, consider the fractionation index defining the fraction of a released compound arriving at the sea surface $F_{i,s}$, given by

$$F_{i,\,s}=\frac{\left[C_{i,\,\text{atm plane}}-C_{i,\,\text{background}}\right]/\left[C_{std,\,\text{atm plane}}-C_{std,\,\text{background}}\right]}{m_{i,\,\text{MRF}}/m_{std,\,\text{MRF}}} \tag{7}$$

where C is the concentration in the atmosphere of compound i and a reference standard compound (subscript "atm plane" is for a plane passing through the atmospheric plume rising from the fresh oil on the sea surface, "std" is for the reference standard compound, and "background" is for the ambient concentration in the atmosphere away from the spill) and m is the mass of compound i and the reference standard compound in the marine riser fluid sample. Ryerson et al. (2011, 2012) used this method to determine the fraction of several compounds that must have dissolved into the seawater during ascent of gas bubbles and oil droplets through the water column.

Gros et al. (2017) applied this technique to compare TAMOC predictions to the measurements of Ryerson et al. (2011, 2012) in the atmosphere and to measurements taken in the intrusion layers (BP Gulf Science Data, 2016). For the atmospheric data, 2-methylheptane is the reference standard; for the intrusion layers, both methane and benzene were used as standards, defining two different sets of fractionation indices. $F_{i,\,methane}$ was used to compare measurements of ethane, propane, and a component of the dispersant, dioctyl sodium sulfosuccinate (DOSS); $F_{i,benzene}$ was used for the other compounds measured in the intrusion layer.

Figure 11 shows a comparison of the predictions of fractionation indices from TAMOC with measurements in the atmosphere and intrusion layers for the DWH. For the lighter compounds, TAMOC is in good agreement with the measurements. For the long-chain, relatively insoluble compounds in the intrusion layer, the default TAMOC simulation (blue bars in Figure 11) underpredicts the measured fractionation. Essentially,

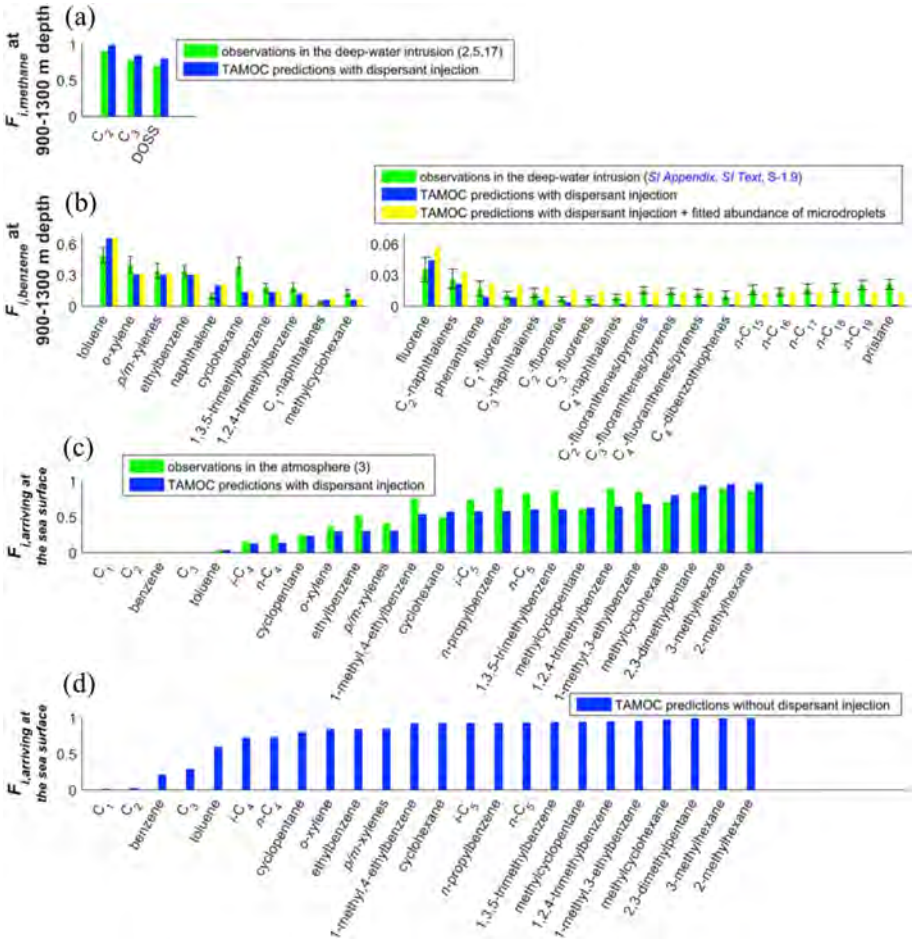

Figure 11. Model predictions by Gros et al. (2017) and reported observations of chemical composition in the deepwater intrusion and at the sea surface during the Deepwater Horizon disaster (4 June to 15 July). (a) Abundances of the readily soluble compounds, C2–C3 and DOSS, in the deepwater hydrocarbon-rich intrusion, expressed as the fraction of mass present in the intrusion relative to that released from the wellhead, normalized to C1. (b) Abundances of semisoluble and sparingly soluble compounds in the deepwater intrusion, expressed as the fraction of mass present in the intrusion relative to that released from the wellhead, normalized to benzene. (c) Abundances of selected volatile organic compounds (VOCs) at the sea surface, assuming dispersant injection, expressed as the fraction of mass arriving at the sea surface relative to that released from the wellhead. (d) TAMOC predictions of the abundances of selected VOCs at the sea surface in the absence of dispersant injection, expressed as the fraction of mass arriving at the sea surface relative to that released from the wellhead. Copyright (2017) National Academy of Sciences (Gros et al., 2017).

the measured data show an occurrence of insoluble petroleum compounds in the intrusion layer, whereas TAMOC, with the initial droplet size distributions from VDROP-J, does not predict any liquid oil in the intrusions at the end of the near-field region. To correct this prediction, Gros et al. (2017) added a small amount of tiny oil droplets (microdroplets with diameters < 130 μm) to the initial oil droplet size distribution and recomputed the simulation. This fraction of microdroplets was based on the original, default simulations and the in situ measured fractionation indices. They estimated a most likely fraction of microdroplets of 1.2% of the released liquid petroleum at the wellhead, with the possible fraction of microdroplet formation spanning 0.6% to 2.0% of the released liquid petroleum. The new simulation results (yellow bars in Figure 11) with microdroplets continue to preserve the TAMOC performance for soluble compounds while also capturing the behavior for these insoluble compounds. Because only the fraction of microdroplets was adjusted and no other model fitting was performed, these data serve as a thorough validation of the modeling algorithms in these integral, droplet, and thermodynamic models.

Validated integral models can also be used to simulate hypothetical scenarios of different response options and blowout scenarios or to estimate the importance of chemical and thermodynamic processes on the plume and intrusion dynamics. Gros et al. (2017) validated their model to data while sub-sea dispersant injection (SSDI) was active. To understand the effect of SSDI, they also reran the simulations without SSDI, assuming the interfacial tension was that of the untreated oil and gas. They showed that oil droplets increased from about 1 mm diameter with SSDI to 4 mm diameter without SSDI; likewise, gas bubbles increased from about 2 mm diameter with SSDI to 9 mm diameter without SSDI. This different size distribution increased the rise rate of the oil droplets and gas bubbles and significantly reduced the dissolution through a reduction in the surface area to volume ratio. In both cases, because the oil droplets rose relatively quickly about 60% of the semivolatile and nonvolatile released mass reached the sea surface; hence, they would not expect a visibly different oil surface slick with or without SSDI. However, the fraction of dissolved compounds in the intrusion layer reduced from 23% with SSDI to only 15% of the released compounds without SSDI. The difference was made up by a slightly higher fraction of dissolution about the intrusion layer without SSDI and by a significant increase (17% without SSDI compared to 13% with SSDI) in rapidly volatilized organic compounds reaching the sea surface and subsequently the atmosphere. This was particularly important for some of the highly toxic BTEX compounds: atmospheric emissions of benzene decreased by 2,000-fold with SSDI relative to simulations without SSDI.

Socolofsky et al. (2015) also considered the effects of SSDI as a blowout response strategy through the use of integral models. In that study, several models available to the government and industry were run for hypothetical scenarios of a subsea oil well blowout in shallow and deepwater, with and without SSDI, and with and without strong ocean currents. Again, the effect of SSDI was simulated by assuming a reduction of the interfacial tension between bubbles and droplets and water. Their study used a gas-rich condensate as the well fluid; however, few models at the time could accurately model the released fluids or the dissolution of mass from the liquid-phase droplets during their ascent through the water column. The assumed oil was also more sensitive to SSDI than the DWH fluid, with an interfacial tension reduction factor of 200 being used in that study. Under these conditions, the conclusions of the study were that industry models for initial droplet size distribution varied by about an order of magnitude for predicted median droplet sizes, all models were fairly robust in their ability to predict the intrusion formation, and most of the transport from deepwater (>1,000 m depth release) occurs as passive Lagrangian particles in the ocean water column.

Finally, in principle, integral models can be used to test the sensitivity of plume dynamics to the complex chemistry and thermodynamics of the real-fluid gas and liquid petroleum bubbles and droplets in the near-field region of the plume. To date, studies with this specific goal have not been published. However, we can deduce some of the answers to these questions from existing published work. The fluids exiting the DWH were elevated in temperature, at least 105°C. Gros et al. (2017) showed that this fluid would cool to 10°C within 7.6 m of the orifice, and all of the VDROP-J and TAMOC simulations conducted in their paper were initialized at 4.3°C. Hence, for predicting the initial bubble and droplet size distributions and the overall near-field dynamics, the heat transfer at the orifice may be neglected. Socolofsky et al. (2015) also compared several different integral models, each using different initial size distributions, different equations-of-state, different compositions of the source oil, and different algorithms to handle the ambient currents. Yet, this diverse set of models predict a trap height of 320 m above the release with a standard deviation of 105 m. Moreover, Socolofsky et al. (2011) could predict the trap height of the DWH using empirical equations that neglect dissolution and crossflows altogether. Hence, trap height is a robust quantity that does not depend strongly on the chemistry or thermodynamics. This is especially the case in deepwater accidents, where the gas expansion by pressure reduction over the height of the near-field plume may be negligible.

8. Conclusions

Jets and plumes have been the focus of quantitative investigations since the pioneering work of the mid 1950s due to their occurrence in a variety of natural and human-made systems, including extensions to multiphase flow. Work on multiphase systems intensified significantly following the DWH accidental oil well blowout in 2010, in which thousands of tons of liquid oil and natural gas were released into the Gulf of Mexico at 1,500 m depth. The present review covered advances on plume dynamics that apply to both

single-phase (i.e., miscible) and multiphase liquid-in-liquid and liquid plus gas into liquid plumes. Major findings reviewed here include the following:

When the gas flow in an oil well is moderate to large, churn flow is likely to occur (Figure 2), and it manifests by major instabilities in the pipe (Montoya et al., 2016). Ignoring the occurrence of churn flow is likely to overestimate the oil discharge of a well and to overestimate the size of oil droplets (Boufadel et al., 2018).

Experiments on oil droplets from jets have been conducted from various orifice sizes (Brandvik et al., 2013; Murphy et al., 2016; Xue & Katz, 2019; Zhao et al., 2017). Xue and Katz (2019) provided observations of composite droplets where small droplets exist within a water bath surrounded by the large droplet. The decrease of pressure at the orifice of a riser is also likely to enhance the release of natural gas from live oil (Pesch et al., 2020), which could cause the expansion of the oil droplets and subsequent bursting if the decrease is large.

Single phase buoyant plumes in stratified ambient fluids have a single intrusion layer (Figure 1b) that depends on the buoyancy properties at the orifice. Multiphase plumes could have multiple intrusion layers that depend also on the slip velocity of individual liquid droplets and/or gas bubbles. This phenomenon explains the large intrusion layer of dissolved hydrocarbon mass observed during the DWH. Given sufficient time, plume precession (off-center gyration) will also occur as long as the rotation of the ambient fluid, due to Coriolis rotation, is not identically equal to zero.

Models for the chemistry of live and dead oil at various depths have been developed and implemented in the TAMOC model. Their implementation allows a complete quantification of hydrocarbon thermodynamics and mass transfer from bubbles and droplets in the water column. Models for oil droplet size distribution from jets/plumes have also been developed. Correlation models were led by Johansen et al. (2013) and a salient population model is VDROP-J (Zhao, Boufadel, et al., 2014). The latter can capture tip streaming due to the application of dispersant, which is manifested by a large number of micron-sized droplets forming downstream of the initial break-up zone.

Models for the initial bubble and droplet size distribution and oil and gas thermodynamics and chemistry have been successfully combined with a multiphase integral-modeling approach to predict the behavior of the near-field region of subsea oil well blowouts. These models agree well with observations during DWH and help confirming the applicability of the bubble- and droplet-scale processes reported here at the field scale.

At the same time, detailed computational fluid dynamic models have been utilized to simulate the centimeter scale hydrodynamics and transport of oil droplets and gas bubbles. These employ diverse approaches to model the multiphase-phase nature of the flow, including both Eulerian-Eulerian and Eulerian-Lagrangian formulations. Both types of models have seen significant advancement in recent years and have the potential to bridge the gap between idealized laboratory and integral models and the real behavior in a dynamical ocean.

While these advances are significant and could not have been realized without the significant resources brought to bear on this problem since DWH, there remain important unknowns requiring further investigation. The success of small-scale plume experiments to predict precession and trap-height formation stems from the fact that dynamic similitude can be achieved between the laboratory analog and the field prototype. In the case of oil and gas breakup into bubbles and droplets at the orifice, this is not the case, and experiments must be conducted at near field-scale to achieve field-scale values of the governing dimensionless parameters. Since field releases of oil and gas are rare and difficult, both from a regulatory and technical point of view, the following areas may yield valuable insight through alternate means.

There is a need to conduct well documented experiments from diameters that are at least 5 to 10 cm, as the maximum droplet diameter, d_{max} (Equation 3) for droplets that can survive in the water is on the order of a centimeter, and thus, orifice diameters smaller than a few centimeter are likely altering the oil droplet size distribution. The large diameter is also needed to reproduce churn flow, which requires diameters on the order of 10 cm. These experiments should include situations where the oil is live and the pressure is large (at water depth of 1,000 m or more) to evaluate the impact of oil degassing. In addition, this series of

experiments should include situations where dispersant is applied to assess the impact and effectiveness of dispersant on the reduction of the oil droplet sizes in the presence of gas at high pressure.

In the existing studies of oil droplet breakup, measurements have been at a single or a few locations and without significant measurement of other plume properties. Detailed new measurements are needed to characterize plume hydrodynamics, oil DSD, and gas bubble size distribution not only at various distances along the center axis of the plume but also at various radial distances. This is needed to understand the kinetics of droplet formation and the key underlying mechanisms. The interaction of these quantities is needed to better assess the mechanisms within multiphase plumes and the breakup models.

New experimental studies should also be accompanied by high fidelity CFD models, especially those relying on LES. In the past, this was difficult since the LES models themselves needed to be developed. Now, these models are in a sufficient level of development that they can be applied synergistically with the measurements. This will help extend the measurement database and will enhance our ability to glean physical insight from both the observations and the simulations.

At the plume scale, two major gaps remain. First, there is no accepted model for bubble- or droplet-generated turbulence, and this term, which adds significant energy to the vertical component of the turbulent fluctuations, is important to the turbulent energy budget of multiphase plumes. Knowing this transfer function is important for turbulence-closure in engineering-scale CFD models (e.g., RANS-based models) and for predicting the energy available to bubble and droplet breakup. Second, the dynamics of multiphase plumes in the combined presence of stratification and crossflow remains illusive. Experiments are expensive and facilities must be large to capture the dynamics above the first intrusion layer formation. CFD models are now able to make predictions in these cases, but validation data is lacking. Though time-average and bulk properties (separation heights, intrusion levels, etc.) have been measured, the mixing dynamics are largely unknown and it remains unclear whether multiple intrusions may form in a stratified crossflow. Measurements during DWH suggest that integral models predicting a single intrusion may be acceptable; however, no laboratory observations exist to corroborate current modeling assumptions.

Each of the new data sets resulting from the above studies should be further used to calibrate and validate engineering-type models, such as VDROP-J and TAMOC, as CFD models are too computationally demanding when the size of the plume exceeds the scale of meters. Hence, to understanding the field-scale behavior, these engineering models will be needed for plume-scale dynamics in the immediate future.

Notations

A_s	surface area of the bubble or droplet, m^2.
BE	breakage efficiency.
B_f	buoyancy flux of the plume, $m^4.s^{-3}$.
C_a	concentration of chemical compound in the seawater, $kg.m^{-3}$.
$C_{s,i}$	solubility of chemical compound in the seawater, $kg.m^{-3}$.
d_e	eddy size, m.
$d_{E,m}$	size of entrained droplet, m.
d_{50}	volume median diameter, m.
d_{max}	maximum stable droplet size, m.
d_{pipe}	pipe diameter, m.
e	energy of an eddy, N.m.
E_c	resistance energy to breakup due to surface tension, N.m.
E_v	resistance energy to breakup due to droplet viscosity, N.m.
f	effective local background rotation, $rad.s^{-1}$.
F_i	fugacity of the ith component in the mixture, Pa.
$F_{i,s}$	fraction of released compound arriving at the sea surface.
g	gravity acceleration, $m.s^{-2}$.
$g(d)$	breakage frequency, s^{-1}.
h	coalescence frequency, s^{-1}.
H	water depth, m.
H_0	Henry's coefficient at standard conditions, $J.mol^{-1}$.

$H_{sol,i}$	enthalpy of solution for the *i*th component of the mixture, J.mol^{-1}.
h_s	separation height, m.
h_P	peel height, m.
h_T	trap height, m.
j_g	gas volumetric flux, m.s^{-1}.
J_0	mass flow rate leaving the mass M_{di}, kg.s^{-1}.
$K_{s,i}$	Setschenow coefficient for the *i*th component of the mixture, L.mol^{-1}.
K_b, c_1, A, B	empirical constants.
L_B	mixing distance of bubble motion, m.
L_D	characteristic distance between bubbles, m.
L_M	jet-to-plume length scale, m.
M_{di}	total droplet mass in size *di*, kg.
$m_{i,\mathrm{MRF}}$	mass of compound *i* in the marine riser fluid, kg.
$m_{std,\mathrm{MRF}}$	mass of the reference standard compound in the marine riser fluid, kg.
M_0	initial momentum flux, m^4.s^{-2}.
M_{sw}	Molecular weight of seawater, kg.mol^{-1}.
n	number concentration of droplets, number of droplets/m^3.
N	buoyancy frequency of the ambient stratification, s^{-1}.
P	in situ pressure, Pa.
P_0	pressure at standard conditions, Pa.
Q_0	initial mixture flow rate, m^3.s^{-1}.
R	universal ideal gas constant, J.mol^{-1}.K^{-1}.
S	in situ salinity, kg.L^{-1}.
S_{ed}	cross-section area between eddy and droplet, m^2.
T	in situ temperature, K.
T_0	temperature at standard conditions, K.
u'	root-mean-square of turbulent velocity, m.s^{-1}.
U_c	centerline velocity along the jet, m.s^{-1}.
u_d	droplet velocity, m.s^{-1}.
u_e	eddy velocity, m.s^{-1}.
U_g^*	dimensionless gas velocity, m.s^{-1}.
U_o	centerline velocity at the orifice, m.s^{-1}.
u_s	slip velocity, m.s^{-1}.
u_{sg}	superficial velocity of gas, m.s^{-1}.
V_i	viscosity number.
$\overline{\mathrm{v}}_\mathrm{i}$	molar volume at infinite dilution of chemical component *i*, m^3.mol^{-1}.

Greek symbols

α	holdup.
β_i	mass transfer coefficient of component *i*, m.s^{-1}.
ε	energy dissipation rate, m^2.s^{-3}.
ρ_c	density of the continuous phase, kg.m^{-3}.
ρ_d	density of the dispersed phase, kg.m^{-3}.
ρ_p	bubble density, kg.m^{-3}.
μ_d	dynamic viscosity of the dispersed phase, kg.m^{-1}s^{-1}.
η	Kolmogorov length scale, m.
Ω	rotation rate of Earth, rad.s^{-1}.
σ	interfacial tension coefficient, N.m^{-1}.
θ	latitude, °.
χ	centerline void fraction.

Dimensionless numbers

F_B	bubble Froude number.

Oh	Ohnesorge number.
Re	Reynolds number.
Ro	Rossby number.
V_i	viscosity number.
$V_{i,G}$	viscosity group.
W_e	Weber number.
W_{ec}	critical Weber number.
$W_{e,d}$	Weber number of entrained droplet.
W_{ev}	Weber number accounts for viscosity.

Glossary of Terminology

Blowout	An accident that results in the release of oil to the environment.
Churn flow	A characteristic flow in a pipe whereby oil and gas tumble violently. The turbulent churn flow creates flow reversals not only along walls but also in recirculation flows around the gas voids.
Clean or dirty bubble	The bubbles surrounded by chemical surfactant over bubble-water interface is called dirty bubble. The surfactant reduces its rise velocity, terminates internal circulations within the bubble, and also reduces the mass transfer rates as internal convection ceases.
Compound droplet	A type of droplet where oil engulfs water droplet containing smaller oil droplets.
Computational fluid dynamics	The prediction of the behavior of fluids and of the effects of fluid motion by numerical methods rather than experiments.
Counter rotating vortex pair	A vortex structure mostly associated with the jets in crossflow. It is a relatively large-scale coherent structure which induces upward velocity near the center plane and downward velocity at sides of the plume.
Dead oil	The crude oil without natural gas (methane) and dissolved hydrocarbons after equilibrium with the atmosphere at standard conditions.
Dispersant	The chemicals that are sprayed on a surface oil slick or applied underwater oil jets/plumes to break down the oil droplets into smaller ones.
Entrainment coefficient	The ratio of lateral entrainment velocity of the ambient fluid to the characteristic axial velocity in the plume.
Eulerian approach	A method in which the flow parameters such as pressure and velocity are described as fields within the control volume.
Holdup	A fraction of one component in a mixture, that is, oil holdup of 0.2 in an oil-gas mixture represents 20% oil and 80% gas in the mixture.
Intrusion layer	A horizontal layer of fluid that is created by the trapping of entrained seawater (including petroleum products) once the buoyancy of the dispersed phase can no longer lift the entrained seawater.
Jet	A body of fluid driven by the momentum of the source.
Lagrangian approach	A method that describes the fluid motion by tracing the path of an individual fluid particle forming the flow.
Live oil	The crude oil with significant gas and volatile compounds dissolved in it.
Oil slick	A film or layer of leaked oil floating on water surface.
Peel height	The height of the plume in a stratified water column where the dispersed phase buoyancy can no longer lift the entrained seawater, and the entrained seawater begins to descend, forming a lateral intrusion layer.
Plume	A body of fluid driven by the buoyancy (density difference between the fluids).
Seep	The leakage of bubbles slowly through the underwater cracks or porous sea floor.
Separation height	The characteristic height of the plume where the gas bubbles and large droplets leaves the plume while its bending in the direction of horizontal currents.

Stratification	Formation of layers of water in the water column with different fluid properties due to the variation of density induced by temperature, salinity etc.
Tip streaming	A mechanism which observed by applying dispersant on oil droplets and generates micron-sized droplets due to the migration of the dispersant to the leeward side of an oil droplet.
Trap height	The neutral buoyancy level at which the entrained seawater (including dissolved petroleum compounds) falls from the peeling height and gets trapped.
Well	A hole drilled or bored into the earth to obtain water, petroleum, natural gas, brine, or sulfur.

Acknowledgments
Funding for this study has come from the Gulf of Mexico Research Initiative, though no official endorsement should be implied. We did not use any new data in this work.

References

Abdelrahim, M. A., & Rao, D. N. (2014). Measurement of interfacial tension in hydrocarbon/water/dispersant systems at deepwater conditions. *Oil Spill Remediation: Colloid Chemistry-Based Principles and Solutions* (pp. 295–315). Hoboken, NJ: John Wiley & Sons, Inc.. https://doi.org/10.1002/9781118825662.ch14

Aiyer, A., Yang, D., Chamecki, M., & Meneveau, C. (2019). A population balance model for large eddy simulation of polydisperse droplet evolution. *Journal of Fluid Mechanics*, *878*, 700–739. https://doi.org/10.1017/jfm.2019.649

Aliseda, A., Bommer, P., Espina, P., Flores, O., Lasheras, J., Lehr, B., et al. (2010). Deepwater Horizon release estimate by PIV, National Incident Command Flow Rate Technical Group.

Anderson, K., Bhatnagar, G., Crosby, D., Hatton, G., Manfield, P., Kuzmicki, A., et al. (2012). Hydrates in the ocean beneath, around, and above production equipment. *Energy & Fuels*, *26*(7), 4167–4176. https://doi.org/10.1021/ef300261z

Anselmet, F., Gagne, Y., Hopfinger, E. J., & Antonia, R. A. (1984). High-order velocity structure functions in turbulent shear flows. *Journal of Fluid Mechanics*, *140*, 63–89. https://doi.org/10.1017/S0022112084000513

Asaeda, T., & Imberger, J. (1993). Structure of bubble plumes in linearly stratified environments. *Journal of Fluid Mechanics*, *249*(1), 35–57. https://doi.org/10.1017/S0022112093001065

Avaullee, L., Trassy, L., Neau, E., & Jaubert, J. N. (1997). Thermodynamic modeling for petroleum fluids I. Equation of state and group contribution for the estimation of thermodynamic parameters of heavy hydrocarbons. *Fluid Phase Equilibria*, *139*(1-2), 155–170. https://doi.org/10.1016/S0378-3812(97)00168-4

Azzopardi, B. J., & Wren, E. (2004). What is entrainment in vertical two-phase churn flow? *International Journal of Multiphase Flow*, *30*(1), 89–103. https://doi.org/10.1016/j.ijmultiphaseflow.2003.11.001

Baldyga, J., & Podgórska, W. (1998). Drop break-up in intermittent turbulence: Maximum stable and transient sizes of drops. *The Canadian Journal of Chemical Engineering*, *76*(3), 456–470. https://doi.org/10.1002/cjce.5450760316

Barbosa, J. Jr., Hewitt, G., König, G., & Richardson, S. (2002). Liquid entrainment, droplet concentration and pressure gradient at the onset of annular flow in a vertical pipe. *International Journal of Multiphase Flow*, *28*(6), 943–961. https://doi.org/10.1016/S0301-9322(02)00003-4

Barnea, D. (1987). A unified model for predicting flow-pattern transitions for the whole range of pipe inclinations. *International Journal of Multiphase Flow*, *13*(1), 1–12. https://doi.org/10.1016/0301-9322(87)90002-4

Bhaga, D., & Weber, M. (1981). Bubbles in viscous liquids: Shapes, wakes and velocities. *Journal of Fluid Mechanics*, *105*(1), 61–85. https://doi.org/10.1017/S002211208100311X

Bolotnov, I. A., Lahey, R. T. Jr., Drew, D. A., & Jansen, K. E. (2008). Turbulent cascade modeling of single and bubbly two-phase turbulent flows. *International Journal of Multiphase Flow*, *34*(12), 1142–1151. https://doi.org/10.1016/j.ijmultiphaseflow.2008.06.006

Bombardelli, F., Buscaglia, G., Rehmann, C., Rincón, L., & García, M. H. (2007). Modeling and scaling of aeration bubble plumes: A two-phase flow analysis. *Journal of Hydraulic Research*, *45*(5), 617–630. https://doi.org/10.1080/00221686.2007.9521798

Boufadel, M. C., Gao, F., Zhao, L., Özgökmen, T., Miller, R., King, T., et al. (2018). Was the Deepwater Horizon well discharge churn flow? Implications on the estimation of the oil discharge and droplet size distribution. *Geophysical Research Letters*, *45*, 2396–2403. https://doi.org/10.1002/2017GL076606

BP Gulf Science Data (2016). Chemistry data associated with water column samples collected in the Gulf of Mexico from May 2010 through July 2012.

Bradshaw, P., Ferriss, D. H., & Johnson, R. (1964). Turbulence in the noise-producing region of a circular jet. *Journal of Fluid Mechanics*, *19*(4), 591–624. https://doi.org/10.1017/S0022112064000945

Brandvik, P. J., Johansen, Ø., Farooq, U., Angell, G., & Leirvik, F. (2014). "Subsurface oil releases—Experimental study of droplet distributions and different dispersant injection techniques Version 2." SINTEF Report No. A26122.

Brandvik, P. J., Johansen, Ø., Leirvik, F., Farooq, U., & Daling, P. S. (2013). Droplet breakup in subsurface oil releases—Part 1: Experimental study of droplet breakup and effectiveness of dispersant injection. *Marine Pollution Bulletin*, *73*(1), 319–326. https://doi.org/10.1016/j.marpolbul.2013.05.020

Bryant, D., Seol, D.-G., & Socolofsky, S. (2009). Quantification of turbulence properties in bubble plumes using vortex identification methods. *Physics of Fluids*, *21*, 075101. https://doi.org/10.1063/1.3176464

Bunner, B., & Tryggvason, G. (2002). Dynamics of homogeneous bubbly flows Part 1. Rise velocity and microstructure of the bubbles. *Journal of Fluid Mechanics*, *466*, 17–52. https://doi.org/10.1017/S0022112002001179

Calabrese, R. V., Chang, T., & Dang, P. (1986). Drop breakup in turbulent stirred-tank contactors. Part 1: Effect of dispersed-phase viscosity. *AICHE Journal*, *32*(4), 657–666. https://doi.org/10.1002/aic.690320416

Cederwall, K., & Ditmars, J. D. (1970). *Analysis of air-bubble plumes*, *W. M. Keck Laboratory of Hydraulics and Water Resources, Division of Engineering and Applied Science* (). Pasadena, CA: California Institute of Technology.

Chan, G. K. Y., Chow, A. C., & Adams, E. E. (2015). Effects of droplet size on intrusion of sub-surface oil spills. *Environmental Fluid Mechanics*, *15*(5), 959–973. https://doi.org/10.1007/s10652-014-9389-5

Chen, B., Yang, D., Meneveau, C., & Chamecki, M. (2016). ENDLESS: An extended nonperiodic domain large-eddy simulation approach for scalar plumes. *Ocean Modelling*, *101*, 121–132. https://doi.org/10.1016/j.ocemod.2016.04.003
Chen, B., Yang, D., Meneveau, C., & Chamecki, M. (2018). Numerical study of the effects of chemical dispersant on oil transport from an idealized underwater blowout. *Physical Review Fluids*, *3*, 083801. https://doi.org/10.1103/PhysRevFluids.3.083801
Chen, F., & Yapa, P. D. (2003). A model for simulating deep water oil and gas blowouts—Part II: Comparison of numerical simulations with "Deepspill" field experiments. *Journal of Hydraulic Research*, *41*(4), 353–365. https://doi.org/10.1080/00221680309499981
Chen, X., & Brill, J. (1997). Slug to churn transition in upward vertical two-phase flow. *Chemical Engineering Science*, *52*(23), 4269–4272. https://doi.org/10.1016/S0009-2509(97)00178-4
Chu, S., & Prosperetti, A. (2017). Bubble plumes in a stratified environment: Source parameters, scaling, intrusion height, and neutral height. *Physical Review Fluids*, *2*, 104503. https://doi.org/10.1103/PhysRevFluids.2.104503
Chu, S., & Prosperetti, A. (2019). Multiphase buoyant plumes with soluble drops or bubbles. *Physical Review Fluids*, *4*, 084306. https://doi.org/10.1103/PhysRevFluids.4.084306
Clift, R., Grace, J. R., & Weber, M. E. (1978). *Bubbles, Drops, and Particles* (). Mineola, New York: Dover Publications.
Coulaloglou, C., & Tavlarides, L. L. (1977). Description of interaction processes in agitated liquid-liquid dispersions. *Chemical Engineering Science*, *32*(11), 1289–1297. https://doi.org/10.1016/0009-2509(77)85023-9
Crounse, B., Wannamaker, E., & Adams, E. (2007). Integral model of a multiphase plume in quiescent stratification. *Journal of Hydraulic Engineering*, *133*(1), 70–76. https://doi.org/10.1061/(ASCE)0733-9429(2007)133:1(70)
Da Hlaing, N., Sirivat, A., Siemanond, K., & Wilkes, J. O. (2007). Vertical two-phase flow regimes and pressure gradients: Effect of viscosity. *Experimental Thermal and Fluid Science*, *31*(6), 567–577. https://doi.org/10.1016/j.expthermflusci.2006.03.030
Danesh, A. (1998). *PVT and Phase Behaviour of Petroleum Reservoir Fluids*. Amsterdam: Elsevier.
De Bruijn, R. A. (1993). Tip streaming of drops in simple shear flows. *Chemical Engineering Science*, *48*(2), 277–284. https://doi.org/10.1016/0009-2509(93)80015-I
Deremble, B. (2016). Convective plumes in rotating systems. *Journal of Fluid Mechanics*, *799*, 27–55. https://doi.org/10.1017/jfm.2016.348
Dhotre, M., Deen, N., Niceno, B., Khan, Z., & Joshi, J. (2013). Large eddy simulation for dispersed bubbly flows: A review. *International Journal of Chemical Engineering*, *2013*, 343276. https://doi.org/10.1155/2013/343276
Dissanayake, A. L., Crowley, C., McCay, D. F., and Mendelohn, D. (2018). Further validation of the unified droplet size distribution model for droplet breakup in underwater plumes. Arctic Marine and Oil Spill Program, AMOP, Edmonton Alberta, Canada.
Dissanayake, A. L., Gros, J., & Socolofsky, S. A. (2018). Integral models for bubble, droplet, and multiphase plume dynamics in stratification and crossflow. *Environmental Fluid Mechanics*, *18*(5), 1167–1202. https://doi.org/10.1007/s10652-018-9591-y
Eastwood, C. D., Armi, L., & Lasheras, J. C. (2004). The breakup of immiscible fluids in turbulent flows. *Journal of Fluid Mechanics*, *502*, 309–333. https://doi.org/10.1017/S0022112003007730
Eggleton, C. D., Tsai, T.-M., & Stebe, K. J. (2001). Tip streaming from a drop in the presence of surfactants. *Physical Review Letters*, *87*(4), 048302. https://doi.org/10.1103/PhysRevLett.87.048302
Fabregat, A., Deremble, B., Wienders, N., Stroman, A., Poje, A., Özgökmen, T., & Dewar, W. (2017). Rotating 2d point source plume models with application to Deepwater Horizon. *Ocean Modelling*, *119*, 118–135. https://doi.org/10.1016/j.ocemod.2017.10.005
Fabregat, A., Dewar, W. K., Özgökmen, T. M., Poje, A. C., & Wienders, N. (2015). Numerical simulations of turbulent thermal, bubble and hybrid plumes. *Ocean Modelling*, *90*, 16–28. https://doi.org/10.1016/j.ocemod.2015.03.007
Fabregat Tomàs, A., Poje, A. C., Özgökmen, T. M., & Dewar, W. K. (2016a). Dynamics of multiphase turbulent plumes with hybrid buoyancy sources in stratified environments. *Physics of Fluids*, *28*, 095109. https://doi.org/10.1063/1.4963313
Fabregat Tomàs, A., Poje, A. C., Özgökmen, T. M., & Dewar, W. K. (2016b). Effects of rotation on turbulent buoyant plumes in stratified environments. *Journal of Geophysical Research: Oceans*, *121*, 5397–5417. https://doi.org/10.1002/2016JC011737
Fabregat Tomàs, A., Poje, A. C., Özgökmen, T. M., & Dewar, W. K. (2017). Numerical simulations of rotating bubble plumes in stratified environments. *Journal of Geophysical Research: Oceans*, *122*, 6795–6813. https://doi.org/10.1002/2017JC013110
Fischer, H. B., List, E. J., Koh, R. C. Y., Imberger, J., & Brooks, N. H. (1979). *Mixing in Inland and Coastal Waters*. New York: Academic Press.
Flores, J. G., Chen, X. T., and Brill, J. P. (1997). Characterization of oil-water flow patterns in vertical and deviated wells. SPE Annual Technical Conference and Exhibition, Society of Petroleum Engineers.
Fraga, B., & Stoesser, T. (2016). Influence of bubble size, diffuser width, and flow rate on the integral behavior of bubble plumes. *Journal of Geophysical Research: Oceans*, *121*, 3887–3904. https://doi.org/10.1002/2015JC011381
Fraga, B., Stoesser, T., Lai, C. C., & Socolofsky, S. A. (2016). A LES-based Eulerian–Lagrangian approach to predict the dynamics of bubble plumes. *Ocean Modelling*, *97*, 27–36. https://doi.org/10.1016/j.ocemod.2015.11.005
Frank, D., Landel, J., Dalziel, S., & Linden, P. (2017). Anticyclonic precession of a plume in a rotating environment. *Geophysical Research Letters*, *44*, 9400–9407. https://doi.org/10.1002/2017GL074191
Fric, T., & Roshko, A. (1994). Vortical structure in the wake of a transverse jet. *Journal of Fluid Mechanics*, *279*, 1–47. https://doi.org/10.1017/S0022112094003800
Friedman, P., & Katz, J. (2002). Mean rise rate of droplets in isotropic turbulence. *Physics of Fluids*, *14*(9), 3059–3073. https://doi.org/10.1063/1.1497377
Frisch, U., & Parisi, G. (1985). Fully developed turbulence and intermittency. In *Turbulence and Predictability in Geophysical Fluid Dynamics and Climate Dynamics* (Vol. 88, pp. 71–88). Amsterdam: North-Holland Publishing Co.
Gao, F., Zhao, L., Boufadel, M., King, T., Robinson, B., Conmy, R., & Miller, R. (2017). Hydrodynamics of oil jets without and with dispersant: Experimental and numerical characterization. *Applied Ocean research*, *68*, 77–90. https://doi.org/10.1016/j.apor.2017.08.013
Garber, J. D., Polaki, V., Adams, C. D., and Varanasi, N. R. (1998). Modeling corrosion rates in non-annular gas condensate wells containing CO_2. CORROSION 98, NACE International.
Gharagheizi, F., Eslamimanesh, A., Mohammadi, A. H., & Richon, D. (2011). Determination of critical properties and acentric factors of pure compounds using the artificial neural network group contribution algorithm. *Journal of Chemical & Engineering Data*, *56*(5), 2460–2476. https://doi.org/10.1021/je200019g
Gopalan, B., & Katz, J. (2010). Turbulent shearing of crude oil mixed with dispersants generates long microthreads and microdroplets. *Physical Review Letters*, *104*, 054501. https://doi.org/10.1103/PhysRevLett.104.054501
Govan, A., Hewitt, G., Richter, H., & Scott, A. (1991). Flooding and churn flow in vertical pipes. *International Journal of Multiphase Flow*, *17*(1), 27–44. https://doi.org/10.1016/0301-9322(91)90068-E

Grace, J., Wairegi, T., & Brophy, J. (1978). Break-up of drops and bubbles in stagnant media. *The Canadian Journal of Chemical Engineering*, *56*(1), 3–8. https://doi.org/10.1002/cjce.5450560101

Gros, J., Dissanayake, A. L., Daniels, M. M., Barker, C. H., Lehr, W., & Socolofsky, S. A. (2018). Oil spill modeling in deep waters: Estimation of pseudo-component properties for cubic equations of state from distillation data. *Marine Pollution Bulletin*, *137*, 627–637. https://doi.org/10.1016/j.marpolbul.2018.10.047

Gros, J., Reddy, C. M., Nelson, R. K., Socolofsky, S. A., & Arey, J. S. (2016). Simulating gas–liquid–water partitioning and fluid properties of petroleum under pressure: Implications for deep-sea blowouts. *Environmental Science & Technology*, *50*(14), 7397–7408. https://doi.org/10.1021/acs.est.5b04617

Gros, J., Socolofsky, S. A., Dissanayake, A. L., Jun, I., Zhao, L., Boufadel, M. C., et al. (2017). Petroleum dynamics in the sea and influence of subsea dispersant injection during Deepwater Horizon. *Proceedings of the National Academy of Sciences*, *114*(38), 10,065–10,070. https://doi.org/10.1073/pnas.1612518114

Hayduk, W., & Laudie, H. (1974). Prediction of diffusion coefficients for nonelectrolytes in dilute aqueous solutions. *AICHE Journal*, *20*(3), 611–615. https://doi.org/10.1002/aic.690200329

Helfrich, K. R., & Battisti, T. M. (1991). Experiments on baroclinic vortex shedding from hydrothermal plumes. *Journal of Geophysical Research*, *96*(C7), 12,511–12,518. https://doi.org/10.1029/90JC02643

Hewitt, G., Martin, C., & Wilkes, N. (1985). Experimental and modelling studies of annular flow in the region between flow reversal and the pressure drop minimum. *Physicochemical Hydrodynamics*, *6*, 43–50.

Hewitt, G. F. (2012). Churn and wispy annular flow regimes in vertical gas–liquid flows. *Energy & Fuels*, *26*(7), 4067–4077. https://doi.org/10.1021/ef3002422

Hewitt, G. F., & Roberts, D. (1969). *Studies of Two-Phase Flow Patterns by Simultaneous X-Ray and Flast Photography*. Harwell, England (United Kingdom): Atomic Energy Research Establishment.

Hine, J., & Mookerjee, P. (1975). The intrinsic hydrophilic character of organic compounds. Correlations in terms of structural contributions. *Journal of Organic Chemistry*, *40*(3), 292–298. https://doi.org/10.1021/jo00891a006

Hinze, J. (1955). Fundamentals of the hydrodynamic mechanism of splitting in dispersion processes. *AICHE Journal*, *1*(3), 289–295. https://doi.org/10.1002/aic.690010303

Hu, G., & Celik, I. (2008). Eulerian–Lagrangian based large-eddy simulation of a partially aerated flat bubble column. *Chemical Engineering Science*, *63*(1), 253–271. https://doi.org/10.1016/j.ces.2007.09.015

Hussein, H. J., Capp, S. P., & George, W. K. (1994). Velocity measurements in a high-Reynolds-number, momentum-conserving, axisymmetric, turbulent jet. *Journal of Fluid Mechanics*, *258*(31-75), 31–75. https://doi.org/10.1017/S002211209400323X

Ishii, M., & Mishima, K. (1989). Droplet entrainment correlation in annular two-phase flow. *International Journal of Heat and Mass Transfer*, *32*(10), 1835–1846. https://doi.org/10.1016/0017-9310(89)90155-5

Jayanti, S., & Hewitt, G. (1992). Prediction of the slug-to-churn flow transition in vertical two-phase flow. *International Journal of Multiphase Flow*, *18*(6), 847–860. https://doi.org/10.1016/0301-9322(92)90063-M

Jirka, G. H. (2004). Integral model for turbulent buoyant jets in unbounded stratified flows. Part I: Single round jet. *Environmental Fluid Mechanics*, *4*(1), 1–56. https://doi.org/10.1023/A:1025583110842

Jirka, G. H., & Domeker, R. L. (1991). Hydrodynamic classification of submerged single-port discharges. *Journal of Hydraulic Engineering*, *117*(9), 1095–1112. https://doi.org/10.1061/(ASCE)0733-9429(1991)117:9(1095)

Johansen, Ø. (2000). DeepBlow—A Lagrangian plume model for deep water blowouts. *Spill Science & Technology Bulletin*, *6*(2), 103–111. https://doi.org/10.1016/S1353-2561(00)00042-6

Johansen, Ø. (2003). Development and verification of deep-water blowout models. *Marine Pollution Bulletin*, *47*(9-12), 360–368. https://doi.org/10.1016/S0025-326X(03)00202-9

Johansen, Ø., Brandvik, P. J., & Farooq, U. (2013). Droplet breakup in subsea oil releases—Part 2: Predictions of droplet size distributions with and without injection of chemical dispersants. *Marine Pollution Bulletin*, *73*(1), 327–335. https://doi.org/10.1016/j.marpolbul.2013.04.012

Johansen, Ø., Rye, H., & Cooper, C. (2003). DeepSpill–-Field study of a simulated oil and gas blowout in deep water. *Spill Science & Technology Bulletin*, *8*(5-6), 433–443. https://doi.org/10.1016/S1353-2561(02)00123-8

Johansen, Ø., Rye, H., Melbye, A. G., Jensen, H. V., Serigstad, B., and Knutsen, T. (2001). "Deep spill JIP-experimental discharges of gas and oil at Helland Hansen-June 2000." Technical Report, DeepSpill JIP, SINTEF, Report No. STF66 F01082.

Johnson, A., Besik, F., & Hamielec, A. (1969). Mass transfer from a single rising bubble. *The Canadian Journal of Chemical Engineering*, *47*(6), 559–564. https://doi.org/10.1002/cjce.5450470615

Kataoka, I., Ishii, M., & Mishima, K. (1983). Generation and size distribution of droplet in annular two-phase flow. *Journal of Fluids Engineering*, *105*(2), 230–238. https://doi.org/10.1115/1.3240969

Kessler, J. D., Valentine, D. L., Redmond, M. C., Du, M., Chan, E. W., Mendes, S. D., et al. (2011). A persistent oxygen anomaly reveals the fate of spilled methane in the deep Gulf of Mexico. *Science*, *331*(6015), 312–315. https://doi.org/10.1126/science.1199697

King, M. B. (1969). *Phase Equilibrium in Mixtures: International Series of Monographs in Chemical Engineering* (). Oxford: Pergamon Press.

Kobus, H. E. (1969). Analysis of the flow induced by air-bubble systems. *Coastal Engineering*, *1968*, 1016–1031.

Krichevsky, I., & Kasarnovsky, J. (1935). Thermodynamical calculations of solubilities of nitrogen and hydrogen in water at high pressures. *Journal of the American Chemical Society*, *57*(11), 2168–2171. https://doi.org/10.1021/ja01314a036

Kytömaa, H., & Brennen, C. (1991). Small amplitude kinematic wave propagation in two-component media. *International Journal of Multiphase Flow*, *17*(1), 13–26. https://doi.org/10.1016/0301-9322(91)90067-D

Lai, C. C., & Socolofsky, S. A. (2019). The turbulent kinetic energy budget in a bubble plume. *Journal of Fluid Mechanics*, *865*, 993–1041. https://doi.org/10.1017/jfm.2019.66

Laın, S., Bröder, D., Sommerfeld, M., & Göz, M. (2002). Modelling hydrodynamics and turbulence in a bubble column using the Euler–Lagrange procedure. *International Journal of Multiphase Flow*, *28*(8), 1381–1407. https://doi.org/10.1016/S0301-9322(02)00028-9

Lance, M., & Bataille, J. (1991). Turbulence in the liquid phase of a uniform bubbly air–water flow. *Journal of Fluid Mechanics*, *222*(1), 95–118. https://doi.org/10.1017/S0022112091001015

Lavelle, J. (1997). Buoyancy-driven plumes in rotating, stratified cross flows: Plume dependence on rotation, turbulent mixing, and cross-flow strength. *Journal of Geophysical Research*, *102*(C2), 3405–3420. https://doi.org/10.1029/96JC03601

Lee, J., & Chu, V. (2003). *Turbulent Jets and Plumes—A Lagrangian Approach* (). Dordrecht, The Netherlands: Kluwer Academics Publishers.

Lee, J. H., & Cheung, V. (1990). Generalized Lagrangian model for buoyant jets in current. *Journal of Environmental Engineering*, *116*(6), 1085–1106. https://doi.org/10.1061/(ASCE)0733-9372(1990)116:6(1085)

Lee, J. H., & Jirka, G. H. (1981). Vertical round buoyant jet in shallow water. *Journal of the Hydraulics Division*, *107*(12), 1651–1675.
Lehr, B., Bristol, S., and Possolo, A. (2010). Oil budget calculator: Deepwater Horizon. Technical documentation. Prepared by the Federal Interagency Solutions Group, Oil Budget Calculator Science and Engineering Team for the National Incident Command.
Leifer, I., Luyendyk, B. P., Boles, J., & Clark, J. F. (2006). Natural marine seepage blowout: Contribution to atmospheric methane. *Global Biogeochemical Cycles*, *20*, GB3008. https://doi.org/10.1029/2005GB002668
Leifer, I., Solomon, E., Schneider, J., Deimling, V., Coffin, R., Rehder, G., & Linke, P. (2015). The fate of bubbles in a large, intense bubble plume for stratified and unstratified water: Numerical simulations of 22/4b expedition field data. *Journal of Marine and Petroleum Geology*, *68B*, 806–823.
Lesieur, M., & Metais, O. (1996). New trends in large-eddy simulations of turbulence. *Annual Review of Fluid Mechanics*, *28*(1), 45–82. https://doi.org/10.1146/annurev.fl.28.010196.000401
Li, H., & Boufadel, M. C. (2010). Long-term persistence of oil from the Exxon Valdez spill in two-layer beaches. *Nature Geoscience*, *3*(2), 96–99. https://doi.org/10.1038/ngeo749
Li, Z., Lee, K., King, T., Boufadel, M. C., and Venosa, A. D. (2008a). Oil droplet size distribution as a function of energy dissipation rate in an experimental wave tank. International Oil Spill Conference, American Petroleum Institute.
Li, Z., Lee, K., King, T., Boufadel, M. C., & Venosa, A. D. (2008b). Assessment of chemical dispersant effectiveness in a wave tank under regular non-breaking and breaking wave conditions. *Marine Pollution Bulletin*, *56*(5), 903–912. https://doi.org/10.1016/j.marpolbul.2008.01.031
Li, Z., Spaulding, M., French McCay, D., Crowley, D., & Payne, J. R. (2017). Development of a unified oil droplet size distribution model with application to surface breaking waves and subsea blowout releases considering dispersant effects. *Marine Pollution Bulletin*, *114*(1), 247–257. https://doi.org/10.1016/j.marpolbul.2016.09.008
Li, Z., and Vinhateiro, N. (2015). "Technical reports for Deepwater Horizon water column injury assessment: Oil particle data from the Deepwater Horizon oil spill." RPS ASA, South Kingstown, RI.
Liao, Y., & Lucas, D. (2010). A literature review on mechanisms and models for the coalescence process of fluid particles. *Chemical Engineering Science*, *65*(10), 2851–2864. https://doi.org/10.1016/j.ces.2010.02.020
Lin, H., & Duan, Y.-Y. (2005). Empirical correction to the Peng–Robinson equation of state for the saturated region. *Fluid Phase Equilibria*, *233*(2), 194–203. https://doi.org/10.1016/j.fluid.2005.05.008
Luo, H., & Svendsen, H. F. (1996). Theoretical model for drop and bubble breakup in turbulent dispersions. *AICHE Journal*, *42*(5), 1225–1233. https://doi.org/10.1002/aic.690420505
MacDonald, I. R., Leifer, I., Sassen, R., Stine, P., Mitchell, R., & Guinasso, N. (2002). Transfer of hydrocarbons from natural seeps to the water column and atmosphere. *Geofluids*, *2*(2), 95–107. https://doi.org/10.1046/j.1468-8123.2002.00023.x
Mahesh, K. (2013). The interaction of jets with crossflow. *Annual Review of Fluid Mechanics*, *45*(1), 379–407. https://doi.org/10.1146/annurev-fluid-120710-101115
Malone, K., Pesch, S., Schlüter, M., & Krause, D. (2018). Oil droplet size distributions in deep-sea blowouts: Influence of pressure and dissolved gases. *Environmental Science & Technology*, *52*(11), 6326–6333. https://doi.org/10.1021/acs.est.8b00587
Martínez-Bazán, C., Montañés, J. L., & Lasheras, J. C. (1999a). On the breakup of an air bubble injected into a fully developed turbulent flow. Part I. Breakup frequency. *Journal of Fluid Mechanics*, *401*, 157–182. https://doi.org/10.1017/S0022112099006680
Martínez-Bazán, C., Montañés, J. L., & Lasheras, J. C. (1999b). On the breakup of an air bubble injected into a fully developed turbulent flow. Part 2. Size PDF of the resulting daughter bubbles. *Journal of Fluid Mechanics*, *401*, 183–207. https://doi.org/10.1017/S0022112099006692
Masutani, S., and Adams, E. (2001). "Experimental study of multiphase plumes with application to deep ocean oil spills, final report." U.S. Department of Interior, Minerals Management Service, Contract No. 1435-01-98-CT-30946.
Mazzitelli, I. M., & Lohse, D. (2009). Evolution of energy in flow driven by rising bubbles. *Physical Review E*, *79*(6), 066317. https://doi.org/10.1103/PhysRevE.79.066317
McCain, W. Jr. (1990). *The Properties of Petroleum Fluids* (second ed.). Tulsa, Oklahoma: PennWell Publishing Company.
McDougall, T. J. (1978). Bubble plumes in stratified environments. *Journal of Fluid Mechanics*, *85*(4), 655–672. https://doi.org/10.1017/S0022112078000841
McGinnis, D. F., Greinert, J., Artemov, Y., Beaubien, S., & Wüest, A. (2006). Fate of rising methane bubbles in stratified waters: How much methane reaches the atmosphere? *Journal of Geophysical Research*, *111*, C09007. https://doi.org/10.1029/2005JC003183
McNeil, D. A., & Stuart, A. D. (2003). The effects of a highly viscous liquid phase on vertically upward two-phase flow in a pipe. *International Journal of Multiphase Flow*, *29*(9), 1523–1549. https://doi.org/10.1016/S0301-9322(03)00122-8
McNutt, M., Camilli, R., Guthrie, G., Hsieh, P., Labson, V., Lehr, B., et al. (2011). Assessment of flow rate estimates for the Deepwater Horizon/Macondo well oil spill. Flow rate technical group report to the national incident command, interagency solutions group, March 10, 2011.
Meneveau, C., & Katz, J. (2000). Scale-invariance and turbulence models for large-eddy simulation. *Annual Review of Fluid Mechanics*, *32*(1), 1–32. https://doi.org/10.1146/annurev.fluid.32.1.1
Meneveau, C., & Sreenivasan, K. R. (1987). The multifractal spectrum of the dissipation field in turbulent flows. *Nuclear Physics B, Proceedings Supplements*, *2*, 49–76. https://doi.org/10.1016/0920-5632(87)90008-9
Michelsen, M. L., & Mollerup, J. (2004). *Thermodynamic Modelling: Fundamentals and Computational Aspects*. Holte, Denmark: Tie-Line Publications.
Milelli, M., B. Smith, and D. Lakehal (2001). Large-eddy simulation of turbulent shear flows laden with bubbles. *Direct and Large-Eddy Simulation IV* (pp. 461–470). Dordrecht: Springer.
Milgram, J. (1983). Mean flow in round bubble plumes. *Journal of Fluid Mechanics*, *133*, 345–376. https://doi.org/10.1017/S0022112083001950
Mitrou, E., Fraga, B., and Stoesser, T. (2018). An Eulerian-Lagrangian numerical method to predict bubbly flows. E3S Web of Conferences, EDP Sciences.
Moin, P., & Mahesh, K. (1998). Direct numerical simulation: A tool in turbulence research. *Annual Review of Fluid Mechanics*, *30*(1), 539–578. https://doi.org/10.1146/annurev.fluid.30.1.539
Montoya, G., Lucas, D., Baglietto, E., & Liao, Y. (2016). A review on mechanisms and models for the churn-turbulent flow regime. *Chemical Engineering Science*, *141*, 86–103. https://doi.org/10.1016/j.ces.2015.09.011
Morton, B., Taylor, G. I., & Turner, J. S. (1956). Turbulent gravitational convection from maintained and instantaneous sources. *Proceedings of the Royal Society of London. Series A: Mathematical and Physical Sciences*, *234*(1196), 1–23.

Murawski, S. A., Ainsworth, C. H., Gilbert, S., Hollander, D. J., Paris, C. B., Schlüter, M., & Wetzel, D. L. (2019). *Deep Oil Spills: Facts, Fate, and Effects* (). Cham, Switzerland: Springer.
Murphy, D. W., Xue, X., Sampath, K., & Katz, J. (2016). Crude oil jets in crossflow: Effects of dispersant concentration on plume behavior. *Journal of Geophysical Research: Oceans*, *121*, 4264–4281. https://doi.org/10.1002/2015JC011574
Narsimhan, G., Gupta, J. P., & Ramkrishna, D. (1979). A model for transitional breakage probability of droplets in agitated lean liquid-liquid dispersions. *Chemical Engineering Science*, *34*(2), 257–265. https://doi.org/10.1016/0009-2509(79)87013-X
National Academies of Sciences Engineering Medicine (NASEM) (2019). *The Use of Dispersants in Marine Oil Spill Response* (). Washington, DC: The National Academies Press.
National Research Council of the National Academies (2013). *An Ecosystem Services Approach to Assessing the Impacts of the Deepwater Horizon Oil Spill in the Gulf of Mexico* (). Washington, DC: National Academies Press.
Navarro, M. A. (2005). Study of countercurrent flow limitation in a horizontal pipe connected to an inclined one. *Nuclear Engineering and Design*, *235*(10-12), 1139–1148. https://doi.org/10.1016/j.nucengdes.2005.02.010
Neto, I. E. L., Zhu, D. Z., & Rajaratnam, N. (2008). Bubbly jets in stagnant water. *International Journal of Multiphase Flow*, *34*(12), 1130–1141. https://doi.org/10.1016/j.ijmultiphaseflow.2008.06.005
Ničeno, B., Boucker, M., & Smith, B. (2009). Euler-Euler large eddy simulation of a square cross-sectional bubble column using the Neptune_CFD code. *Science and Technology of Nuclear Installations*, *2009*, 410272. https://doi.org/10.1155/2009/410272
North, E. W., Adams, E. E., Schlag, Z., Sherwood, C. R., He, R., Hyun, K. H., & Socolofsky, S. A. (2011). *Simulating Oil Droplet Dispersal From the Deepwater Horizon Spill With a Lagrangian Approach*, *Geophysical Monograph Series* (Vol. 195, pp. 217–226). Washington, DC: American Geophysical Union.
North, E. W., Adams, E. E., Thessen, A. E., Schlag, Z., He, R., Socolofsky, S. A., et al. (2015). The influence of droplet size and biodegradation on the transport of subsurface oil droplets during the Deepwater Horizon spill: A model sensitivity study. *Environmental Research Letters*, *10*, 024016. https://doi.org/10.1088/1748-9326/10/2/024016
Orell, A., & Rembrand, R. (1986). A model for gas-liquid slug flow in a vertical tube. *Industrial and Engineering Chemistry Fundamentals*, *25*(2), 196–206. https://doi.org/10.1021/i100022a004
Ouro, P., Fraga, B., Lopez-Novoa, U., & Stoesser, T. (2019). Scalability of an Eulerian-Lagrangian large-eddy simulation solver with hybrid MPI/OpenMP parallelisation. *Computers & Fluids*, *179*, 123–136. https://doi.org/10.1016/j.compfluid.2018.10.013
Pan, Z., Zhao, L., Boufadel, M. C., King, T., Robinson, B., Conmy, R., & Lee, K. (2016). Impact of mixing time and energy on the dispersion effectiveness and droplets size of oil. *Chemosphere*, *166*, 246–254. https://doi.org/10.1016/j.chemosphere.2016.09.052
Parsi, M., Vieira, R. E., Torres, C. F., Kesana, N. R., McLaury, B. S., Shirazi, S. A., et al. (2015a). Experimental investigation of interfacial structures within churn flow using a dual wire-mesh sensor. *International Journal of Multiphase Flow*, *73*, 155–170. https://doi.org/10.1016/j.ijmultiphaseflow.2015.03.019
Parsi, M., Vieira, R. E., Torres, C. F., Kesana, N. R., McLaury, B. S., Shirazi, S. A., et al. (2015b). On the effect of liquid viscosity on interfacial structures within churn flow: Experimental study using wire mesh sensor. *Chemical Engineering Science*, *130*, 221–238. https://doi.org/10.1016/j.ces.2015.03.033
Patton, J. S., Rigler, M. W., Boehm, P. D., & Fiest, D. L. (1981). Ixtoc I oil spill: Flaking of surface mousse in the Gulf of Mexico. *Nature*, *290*(5803), 1235–1238.
Pedersen, K. S., Christensen, P. L., & Shaikh, J. A. (2014). *Phase Behavior of Petroleum Reservoir Fluids* (). Boca. Raton, FL: CRC Press.
Peng, D.-Y., & Robinson, D. B. (1976). A new two-constant equation of state. *Industrial and Engineering Chemistry Fundamentals*, *15*(1), 59–64. https://doi.org/10.1021/i160057a011
Pesch, S., Schlüter, M., Aman, Z. M., Malone, K., Krause, D., & Paris, C. B. (2020). *Behavior of Rising Droplets and Bubbles: Impact on the Physics of Deep-Sea Blowouts and Oil Fate. Deep Oil Spills* (pp. 65–82). Switzerland: Springer.
Plume Calculation Team (2010). *Deepwater Horizon Release Estimate of Rate by PIV* (). Washington, DC: U.S. Department of the Interior.
Poling, B. E., Prausnitz, J. M., & O'Connell, J. P. (2001). *The Properties of Gases and Liquids* (). New York: McGraw-Hill.
Pope, S. (2000). *Turbulent Flows* (). Cambridge, New York: Cambridge University Press.
Premathilake, L. T., Yapa, P. D., Nissanka, I. D., & Kumarage, P. (2016). Modeling the flow regime near the source in underwater gas releases. *Journal of Marine Science and Application*, *15*(4), 433–441. https://doi.org/10.1007/s11804-016-1376-4
Prince, M. J., & Blanch, H. W. (1990). Bubble coalescence and break-up in air-sparged bubble columns. *AICHE Journal*, *36*(10), 1485–1499. https://doi.org/10.1002/aic.690361004
Prince, R. C., Butler, J. D., & Redman, A. D. (2017). The rate of crude oil biodegradation in the sea. *Environmental Science & Technology*, *51*(3), 1278–1284. https://doi.org/10.1021/acs.est.6b03207
Privat, R., & Jaubert, J.-N. (2012). Addition of the sulfhydryl group (SH) to the PPR78 model: Estimation of missing group-interaction parameters for systems containing mercaptans and carbon dioxide or nitrogen or methane, from newly published data. *Fluid Phase Equilibria*, *334*, 197–203. https://doi.org/10.1016/j.fluid.2012.08.007
Reddy, C. M., Arey, J. S., Seewald, J. S., Sylva, S. P., Lemkau, K. L., Nelson, R. K., et al. (2012). Composition and fate of gas and oil released to the water column during the Deepwater Horizon oil spill. *Proceedings of the National Academy of Sciences*, *109*(50), 20,229–20,234. https://doi.org/10.1073/pnas.1101242108
Reddy, C. M., Eglinton, T. I., Hounshell, A., White, H. K., Xu, L., Gaines, R. B., & Frysinger, G. S. (2002). The west Falmouth oil spill after thirty years: The persistence of petroleum hydrocarbons in marsh Sediments. *Environmental Science & Technology*, *36*(22), 4754–4760. https://doi.org/10.1021/es020656n
Rensen, J., Luther, S., & Lohse, D. (2005). The effect of bubbles on developed turbulence. *Journal of Fluid Mechanics*, *538*(1), 153–187. https://doi.org/10.1017/S0022112005005276
Rensen, J., & Roig, V. (2001). Experimental study of the unsteady structure of a confined bubble plume. *International Journal of Multiphase Flow*, *27*(8), 1431–1449. https://doi.org/10.1016/S0301-9322(01)00012-X
Robinson, D. B., and Peng, D.-Y. (1978). The characterization of the heptanes and heavier fractions for the GPA Peng-Robinson programs, Gas processors association.
Roghair, I., Mercado, J. M., Annaland, M. V. S., Kuipers, H., Sun, C., & Lohse, D. (2011). Energy spectra and bubble velocity distributions in pseudo-turbulence: Numerical simulations vs. experiments. *International Journal of Multiphase Flow*, *37*(9), 1093–1098. https://doi.org/10.1016/j.ijmultiphaseflow.2011.07.004
Ryerson, T., Aikin, K., Angevine, W., Atlas, E. L., Blake, D., Brock, C., et al. (2011). Atmospheric emissions from the Deepwater Horizon spill constrain air-water partitioning, hydrocarbon fate, and leak rate. *Geophysical Research Letters*, *38*, L07803. https://doi.org/10.1029/2011GL046726

Ryerson, T. B., Camilli, R., Kessler, J. D., Kujawinski, E. B., Reddy, C. M., Valentine, D. L., et al. (2012). Chemical data quantify Deepwater Horizon hydrocarbon flow rate and environmental distribution. *Proceedings of the National Academy of Sciences*, *109*(50), 20,246–20,253. https://doi.org/10.1073/pnas.1110564109

Schmidt, J., Giesbrecht, H., & Van Der Geld, C. (2008). Phase and velocity distributions in vertically upward high-viscosity two-phase flow. *International Journal of Multiphase Flow*, *34*(4), 363–374. https://doi.org/10.1016/j.ijmultiphaseflow.2007.10.013

Seol, D.-G., Bhaumik, T., Bergmann, C., & Socolofsky, S. A. (2007). Particle image velocimetry measurements of the mean flow characteristics in a bubble plume. *Journal of Engineering Mechanics*, *133*(6), 665–676. https://doi.org/10.1061/(ASCE)0733-9399(2007)133:6(665)

Seol, D.-G., Bryant, D. B., & Socolofsky, S. A. (2009). Measurement of behavioral properties of entrained ambient water in a stratified bubble plume. *Journal of Hydraulic Engineering*, *135*(11), 983–988. https://doi.org/10.1061/(ASCE)HY.1943-7900.0000109

Seol, D.-G., & Socolofsky, S. A. (2008). Vector post-processing algorithm for phase discrimination of two-phase PIV. *Experiments in Fluids*, *45*(2), 223–239. https://doi.org/10.1007/s00348-008-0473-9

Shah, Y., Kelkar, B. G., Godbole, S., & Deckwer, W. D. (1982). Design parameters estimations for bubble column reactors. *AICHE Journal*, *28*(3), 353–379. https://doi.org/10.1002/aic.690280302

Simiano, M., Zboray, R., De Cachard, F., Lakehal, D., & Yadigaroglu, G. (2006). Comprehensive experimental investigation of the hydrodynamics of large-scale, 3D, oscillating bubble plumes. *International Journal of Multiphase Flow*, *32*(10-11), 1160–1181. https://doi.org/10.1016/j.ijmultiphaseflow.2006.05.014

Sleicher, C. (1962). Maximum stable drop size in turbulent flow. *AICHE Journal*, *8*(4), 471–477. https://doi.org/10.1002/aic.690080410

Socolofsky, S., & Adams, E. (2002). Multi-phase plumes in uniform and stratified crossflow. *Journal of Hydraulic Research*, *40*(6), 661–672. https://doi.org/10.1080/00221680209499913

Socolofsky, S., & Rehmann, C. (2013). Bubble plumes. In *Handbook of Environmental Fluid Dynamics, Volume Two* (pp. 55–67). New York: CRC Press.

Socolofsky, S. A., & Adams, E. E. (2003). Liquid volume fluxes in stratified multiphase plumes. *Journal of Hydraulic Engineering*, *129*(11), 905–914. https://doi.org/10.1061/(ASCE)0733-9429(2003)129:11(905)

Socolofsky, S. A., & Adams, E. E. (2005). Role of slip velocity in the behavior of stratified multiphase plumes. *Journal of Hydraulic Engineering*, *131*(4), 273–282. https://doi.org/10.1061/(ASCE)0733-9429(2005)131:4(273)

Socolofsky, S. A., Adams, E. E., Boufadel, M. C., Aman, Z. M., Johansen, Ø., Konkel, W. J., et al. (2015). Intercomparison of oil spill prediction models for accidental blowout scenarios with and without subsea chemical dispersant injection. *Marine Pollution Bulletin*, *96*(1-2), 110–126. https://doi.org/10.1016/j.marpolbul.2015.05.039

Socolofsky, S. A., Adams, E. E., & Sherwood, C. R. (2011). Formation dynamics of subsurface hydrocarbon intrusions following the Deepwater Horizon blowout. *Geophysical Research Letters*, *38*, L09602. https://doi.org/10.1029/2011GL047174

Socolofsky, S. A., Bhaumik, T., & Seol, D.-G. (2008). Double-plume integral models for near-field mixing in multiphase plumes. *Journal of Hydraulic Engineering*, *134*(6), 772–783. https://doi.org/10.1061/(ASCE)0733-9429(2008)134:6(772)

Socolofsky, S. A., Crounse, B. C., & Adams, E. E. (2002). Multiphase plumes in uniform, stratified, and flowing environments. *Environmental Fluid Mechanics Theories and Applications* (pp. 85–125). Reston, VA: ASCE.

Socolofsky, S. A., Gros, J., North, E., Boufadel, M. C., Parkerton, T. F., & Adams, E. E. (2019). The treatment of biodegradation in models of sub-surface oil spills: A review and sensitivity study. *Marine Pollution Bulletin*, *143*, 204–219. https://doi.org/10.1016/j.marpolbul.2019.04.018

Sokolichin, A., Eigenberger, G., Lapin, A., & Lübert, A. (1997). Dynamic numerical simulation of gas-liquid two-phase flows Euler/Euler versus Euler/Lagrange. *Chemical Engineering Science*, *52*(4), 611–626. https://doi.org/10.1016/S0009-2509(96)00425-3

Spaulding, M., Li, Z., Mendelsohn, D., Crowley, D., French-McCay, D., & Bird, A. (2017). Application of an integrated blowout model system, OILMAP DEEP, to the Deepwater Horizon (DWH) spill. *Marine Pollution Bulletin*, *120*(1-2), 37–50. https://doi.org/10.1016/j.marpolbul.2017.04.043

Spier, C., Stringfellow, W. T., Hazen, T. C., & Conrad, M. (2013). Distribution of hydrocarbons released during the 2010 MC252 oil spill in deep offshore waters. *Environmental Pollution*, *173*, 224–230. https://doi.org/10.1016/j.envpol.2012.10.019

Stevens, C. C., Thibodeaux, L. J., Overton, E. B., Valsaraj, K. T., Nandakumar, K., Rao, A., & Walker, N. D. (2015). Sea surface oil slick light component vaporization and heavy residue sinking: Binary mixture theory and experimental proof of concept. *Environmental Engineering Science*, *32*(8), 694–702. https://doi.org/10.1089/ees.2015.0022

Sun, T. Y., & Faeth, G. M. (1986). Structure of turbulent bubbly jets—II. Phase property profiles. *International Journal of Multiphase Flow*, *12*(1), 115–126. https://doi.org/10.1016/0301-9322(86)90007-8

Sungkorn, R., Derksen, J., & Khinast, J. (2011). Modeling of turbulent gas–liquid bubbly flows using stochastic Lagrangian model and lattice-Boltzmann scheme. *Chemical Engineering Science*, *66*(12), 2745–2757. https://doi.org/10.1016/j.ces.2011.03.032

Tomiyama, A., Celata, G., Hosokawa, S., & Yoshida, S. (2002). Terminal velocity of single bubbles in surface tension force dominant regime. *International Journal of Multiphase Flow*, *28*(9), 1497–1519. https://doi.org/10.1016/S0301-9322(02)00032-0

Tseng, Y.-H., & Prosperetti, A. (2015). Local interfacial stability near a zero vorticity point. *Journal of Fluid Mechanics*, *776*, 5–36. https://doi.org/10.1017/jfm.2015.246

Tsouris, C., & Tavlarides, L. L. (1994). Breakage and coalescence models for drops in turbulent dispersions. *AICHE Journal*, *40*(3), 395–406. https://doi.org/10.1002/aic.690400303

Turner, J. (1986). Turbulent entrainment: The development of the entrainment assumption, and its application to geophysical flows. *Journal of Fluid Mechanics*, *173*, 431–471. https://doi.org/10.1017/S0022112086001222

Ulivieri, G., Ripepe, M., & Marchetti, E. (2013). Infrasound reveals transition to oscillatory discharge regime during lava fountaining: Implication for early warning. *Geophysical Research Letters*, *40*, 3008–3013. https://doi.org/10.1002/grl.50592

van Nimwegen, A. T., Portela, L. M., & Henkes, R. A. W. M. (2015). The effect of surfactants on air–water annular and churn flow in vertical pipes. Part 1: Morphology of the air–water interface. *International Journal of Multiphase Flow*, *71*, 133–145. https://doi.org/10.1016/j.ijmultiphaseflow.2014.03.008

Wallis, G. B. (1969). *One-Dimensional Two-Phase Flow* (). New York: McGraw-Hill.

Waltrich, P. J., Falcone, G., & Barbosa, J. R. Jr. (2013). Axial development of annular, churn and slug flows in a long vertical tube. *International Journal of Multiphase Flow*, *57*, 38–48. https://doi.org/10.1016/j.ijmultiphaseflow.2013.06.008

Wang, B., Lai, C. C., & Socolofsky, S. A. (2019). Mean velocity, spreading and entrainment characteristics of weak bubble plumes in unstratified and stationary water. *Journal of Fluid Mechanics*, *874*, 102–130. https://doi.org/10.1017/jfm.2019.461

Wang, B., & Socolofsky, S. A. (2015). A deep-sea, high-speed, stereoscopic imaging system for in situ measurement of natural seep bubble and droplet characteristics. *Deep Sea Research Part I: Oceanographic Research Papers*, *104*, 134–148. https://doi.org/10.1016/j.dsr.2015.08.001

Wang, B., Socolofsky, S. A., Breier, J. A., & Seewald, J. S. (2016). Observations of bubbles in natural seep flares at MC 118 and GC 600 using in situ quantitative imaging. *Journal of Geophysical Research: Oceans*, *121*, 2203–2230. https://doi.org/10.1002/2015JC011452

Wang, B., Socolofsky, S. A., Lai, C. C., Adams, E. E., & Boufadel, M. C. (2018). Behavior and dynamics of bubble breakup in gas pipeline leaks and accidental subsea oil well blowouts. *Marine Pollution Bulletin*, *131*(Pt A), 72–86. https://doi.org/10.1016/j.marpolbul.2018.03.053

Wang, C., & Calabrese, R. V. (1986). Drop breakup in turbulent stirred-tank contactors. Part II: Relative influence of viscosity and interfacial tension. *AICHE Journal*, *32*(4), 667–676. https://doi.org/10.1002/aic.690320417

Wang, D., & Adams, E. E. (2016). Intrusion dynamics of particle plumes in stratified water with weak crossflow: Application to deep ocean blowouts. *Journal of Geophysical Research: Oceans*, *121*, 3820–3835. https://doi.org/10.1002/2015JC011324

Wang, K., Bai, B., & Ma, W. (2013). A model for droplet entrainment in churn flow. *Chemical Engineering Science*, *104*, 1045–1055. https://doi.org/10.1016/j.ces.2013.10.028

Wang, T., & Wang, J. (2007). Numerical simulations of gas–liquid mass transfer in bubble columns with a CFD–PBM coupled model. *Chemical Engineering Science*, *62*(24), 7107–7118. https://doi.org/10.1016/j.ces.2007.08.033

Warzinski, R. P., Lynn, R., Haljasmaa, I., Leifer, I., Shaffer, F., Anderson, B. J., & Levine, J. S. (2014). Dynamic morphology of gas hydrate on a methane bubble in water: Observations and new insights for hydrate film models. *Geophysical Research Letters*, *41*, 6841–6847. https://doi.org/10.1002/2014GL061665

Weisman, J. (1983). Chapter 15 Two-phase flow patterns. In *Handbook of Fluids in Motion* (pp. 409–425). Ann Arbor, Michigan: Ann Arbor Science.

Whitehead, J., Marshall, J., & Hufford, G. E. (1996). Localized convection in rotating stratified fluid. *Journal of Geophysical Research*, *101*(C11), 25,705–25,721. https://doi.org/10.1029/96JC02322

Woods, A. W. (2010). Turbulent plumes in nature. *Annual Review of Fluid Mechanics*, *42*(1), 391–412. https://doi.org/10.1146/annurev-fluid-121108-145430

Wu, M., & Gharib, M. (2002). Experimental studies on the shape and path of small air bubbles rising in clean water. *Physics of Fluids*, *14*(7), L49–L52. https://doi.org/10.1063/1.1485767

Wüest, A., Brooks, N. H., & Imboden, D. M. (1992). Bubble plume modeling for lake restoration. *Water Resources Research*, *28*(12), 3235–3250. https://doi.org/10.1029/92WR01681

Wygnanski, I., & Fiedler, H. E. (1969). Some measurements in the self-preserving jet. *Journal of Fluid Mechanics*, *38*(3), 577–612. https://doi.org/10.1017/S0022112069000358

Xue, X., & Katz, J. (2019). Formation of compound droplets during fragmentation of turbulent buoyant oil jet in water. *Journal of Fluid Mechanics*, *878*, 98–112. https://doi.org/10.1017/jfm.2019.645

Yang, D., Chen, B., Socolofsky, S. A., Chamecki, M., & Meneveau, C. (2016). Large-eddy simulation and parameterization of buoyant plume dynamics in stratified flow. *Journal of Fluid Mechanics*, *794*, 798–833. https://doi.org/10.1017/jfm.2016.191

Yang, X., Zhang, X., Li, Z., & He, G.-W. (2009). A smoothing technique for discrete delta functions with application to immersed boundary method in moving boundary simulations. *Journal of Computational Physics*, *228*(20), 7821–7836. https://doi.org/10.1016/j.jcp.2009.07.023

Yapa, P. D., & Li, Z. (1997). Simulation of oil spills from underwater accidents I: Model development. *Journal of Hydraulic Research*, *35*(5), 673–688. https://doi.org/10.1080/00221689709498401

Yapa, P. D., & Xie, H. (2002). Modeling underwater oil/gas jets and plumes: Comparison with field data. *Journal of Hydraulic Engineering*, *128*(9), 855–860. https://doi.org/10.1061/(ASCE)0733-9429(2002)128:9(855)

Yapa, P. D., & Zheng, L. (1997). Modelling oil and gas releases from deep water: A review. *Spill Science & Technology Bulletin*, *4*(4), 189–198. https://doi.org/10.1016/S1353-2561(98)00020-6

Zhao, L., Boufadel, M. C., Adams, E. E., Socolofsky, S., King, T., & Lee, K. (2015). Simulation of scenarios of oil droplet formation from the Deepwater Horizon blowout. *Marine Pollution Bulletin*, *101*(1), 304–319. https://doi.org/10.1016/j.marpolbul.2015.10.068

Zhao, L., Boufadel, M. C., King, T., Robinson, B., Conmy, R., & Lee, K. (2018). Impact of particle concentration and out-of-range sizes on the measurements of the LISST. *Measurement Science and Technology*, *29*, 055302. https://doi.org/10.1088/1361-6501/aab83d

Zhao, L., Boufadel, M. C., Lee, K., King, T., Loney, N., & Geng, X. (2016). Evolution of bubble size distribution from gas blowout in shallow water. *Journal of Geophysical Research: Oceans*, *121*, 1573–1599. https://doi.org/10.1002/2015JC011403

Zhao, L., Boufadel, M. C., Socolofsky, S. A., Adams, E., King, T., & Lee, K. (2014). Evolution of droplets in subsea oil and gas blowouts: Development and validation of the numerical model VDROP-J. *Marine Pollution Bulletin*, *83*(1), 58–69. https://doi.org/10.1016/j.marpolbul.2014.04.020

Zhao, L., Gao, F., Boufadel, M. C., King, T., Robinson, B., Lee, K., & Conmy, R. (2017). Oil jet with dispersant: Macro-scale hydrodynamics and tip streaming. *AICHE Journal*, *63*(11), 5222–5234. https://doi.org/10.1002/aic.15864

Zhao, L., Shaffer, F., Robinson, B., King, T., D'Ambrose, C., Pan, Z., et al. (2016). Underwater oil jet: Hydrodynamics and droplet size distribution. *Chemical Engineering Journal*, *299*, 292–303. https://doi.org/10.1016/j.cej.2016.04.061

Zhao, L., Torlapati, J., Boufadel, M. C., King, T., Robinson, B., & Lee, K. (2014). VDROP: A comprehensive model for droplet formation of oils and gases in liquids-Incorporation of the interfacial tension and droplet viscosity. *Chemical Engineering Journal*, *253*, 93–106. https://doi.org/10.1016/j.cej.2014.04.082

Zhao, Y., Yeung, H., Zorgani, E., Archibong, A., & Lao, L. (2013). High viscosity effects on characteristics of oil and gas two-phase flow in horizontal pipes. *Chemical Engineering Science*, *95*, 343–352. https://doi.org/10.1016/j.ces.2013.03.004

Zheng, L., & Yapa, P. D. (1998). Simulation of oil spills from underwater accidents II: Model verification. *Journal of Hydraulic Research*, *36*(1), 117–134. https://doi.org/10.1080/00221689809498381

Zheng, L., & Yapa, P. D. (2002). Modeling gas dissolution in deepwater oil/gas spills. *Journal of Marine Systems*, *31*(4), 299–309. https://doi.org/10.1016/S0924-7963(01)00067-7

Zheng, L., Yapa, P. D., & Chen, F. (2003). A model for simulating deepwater oil and gas blowouts—Part I: Theory and model formulation. *Journal of Hydraulic Research*, *41*(4), 339–351. https://doi.org/10.1080/00221680309499980

Zick, A. (2013). "Equation-of-state fluid characterization and analysis of the Macondo reservoir fluids." Expert report prepared on behalf of the United States.